DANMARKS OG GRØNLANDS GEOLOGISKE UNDERSØGELSE RAPPORT 2019/7

ASTER data analysis applied to mineral and geological mapping in North East Greenland

Documentation of the NEG ASTER Project

Sara Salehi, Símun D. Olsen, Christian B. Pedersen
& Leif Thorning

GEOLOGICAL SURVEY OF DENMARK AND GREENLAND
DANISH MINISTRY OF ENERGY, UTILITIES AND CLIMATE

G E U S

DANMARKS OG GRØNLANDS GEOLOGISKE UNDERSØGELSE RAPPORT 2019/7

ASTER data analysis applied to mineral and geological mapping in North East Greenland

Documentation of the NEG ASTER Project

Sara Salehi, Símun D. Olsen, Christian B. Pedersen
& Leif Thorning

GEOLOGICAL SURVEY OF DENMARK AND GREENLAND
DANISH MINISTRY OF ENERGY, UTILITIES AND CLIMATE

GEUS

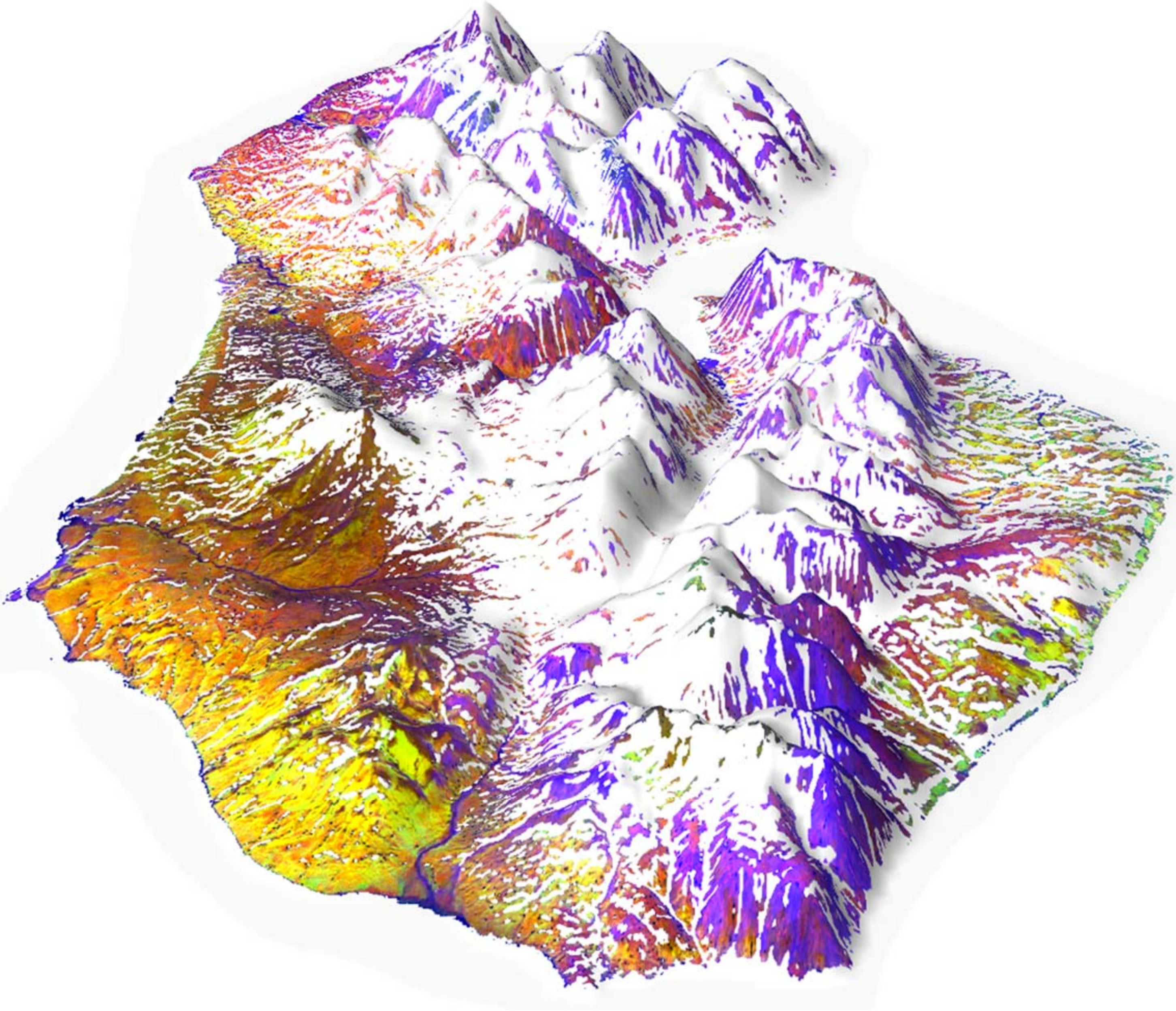

Frontispice: False color composite image highlighting different lithological units of Kuhn Ø (see Figure 26). The image is draped on digital elevation model of the area.

Table of contents

Abbreviations

ASTER	Advanced Spaceborne Thermal Emission and Reflection Radiometer
DEM	Digital Elevation Model
EOS	Earth Observatory System
GEUS	Geological Survey of Denmark and Greenland
MMR	Ministry of Minerals and Resources
MNF	Minimum Noise Fraction
NASA	National Aeronautics and Space Administration
NDVI	Normalized Difference Vegetation Index
PCA	Principal Component Analysis
WMTS	Web Map Tile Service
SWIR	Short-wave infrared
TM	Topographic Map
TIR	Thermal Infrared
VNIR	Visible to near infrared

Figures

Abstract

The purpose of this report is to document the processing of Advanced Spaceborne Thermal Emission and Reflection Radiometer (ASTER) data that has been carried out for primary geological mapping in North East Greenland in the context of NEG ASTER project. The investigated area (73.8° to 75.8° N) is approximately 80.000 km^2 and is covered by 1:1.000.000, 1:500.000 and 1:250.000 scale geological maps (Henriksen 1997, Escher 2001, Henriksen 2003, Christoffersen and Jepsen 2007).
The Ministry of Minerals and Resources (MMR) funded the NEG ASTER project in 2016, where Geological Survey of Denmark and Greenland (GEUS) was tasked to large-scale processing and interpretation of ASTER data in preparation for an upcoming field operation in summer 2018 and with the aim of generating a more detailed geological map sheet (in 1:100.000 scale) from the region. The project is a joint venture with Asiaq, which was contracted to deliver a new detailed Digital Elevation Model (DEM) for the project area. A series of standard ASTER mineral indices (Kalinowski and Oliver 2004) targeting specific spectral absorption features (see Appendix 1) were calculated to improve the geological background knowledge in the area. The resultant images allow to identify the spectral variability and composition within the area covered by scenes. Band ratio color combination images, Principal Component Analysis (PCA) and Minimum Noise Fraction (MNF) methods were used to assign spectral characteristics to variations in lithology in the area.
Altogether 124 scenes were downloaded covering the Hudson Land, Dove Bugt and Dronning Louise Land in North East Greenland (73.3° to 78° N; ~170.000 km^2), see Appendix 3 for the list of downloaded and processed scenes. A spatial subset including twenty-two ASTER scenes from the region around Hudson Land (73.8° to 75.8° N; ~80.000 km^2) was selected for further analysis (Figure 1). The first stage of the project started with a test study around Wollaston Forland and processing of only three ASTER scenes. The results were made available by mid-June 2018 for the field participants in summer. The remaining 19 scenes and the related products were delivered on February 2019.

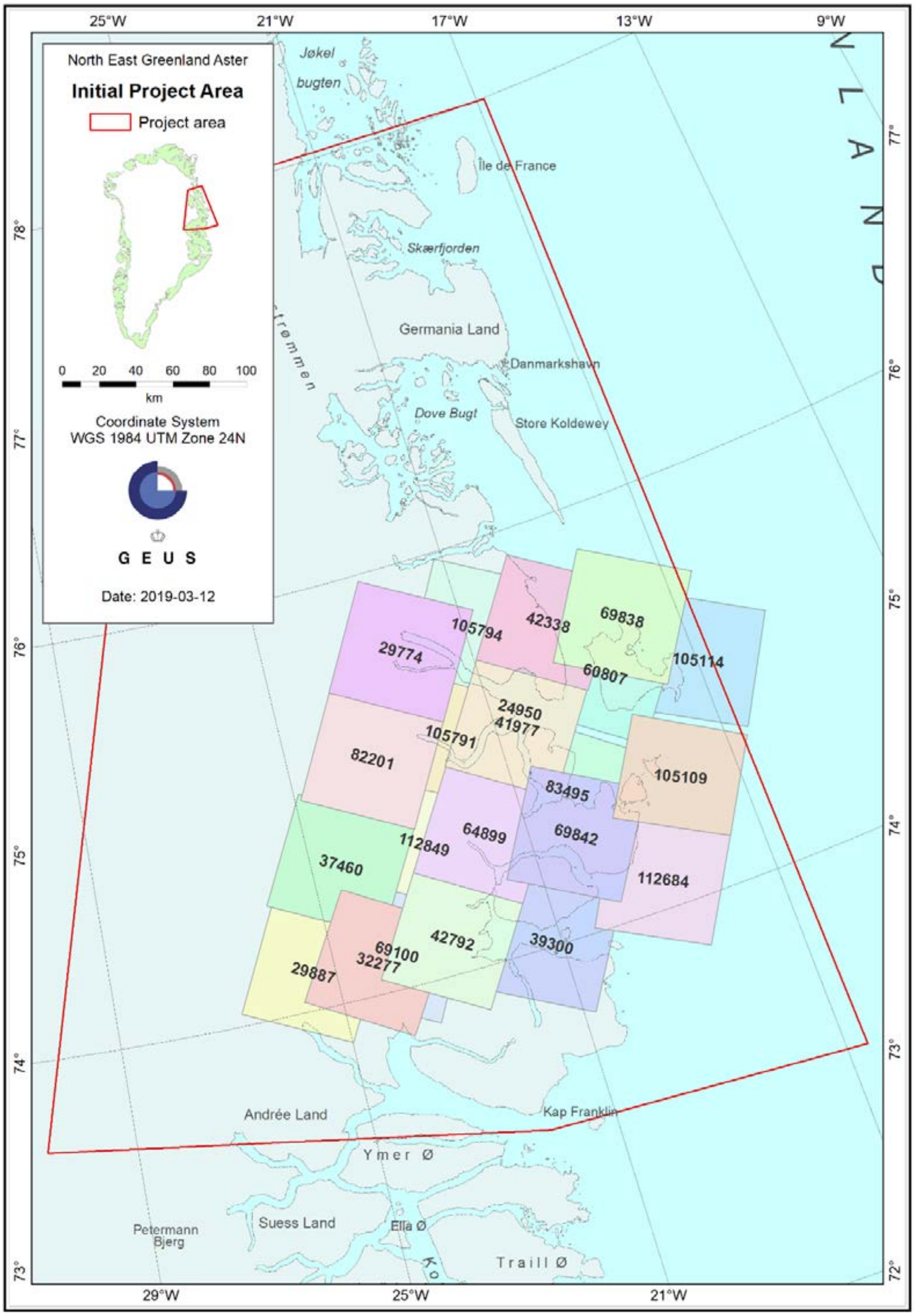

Figure 1. The initial project area, shown with red polygon, is divided into three spatial subsets; namely Hudson Land, Dove Bugt and Dronning Louise Land. The 24 processed ASTER scenes and their footprints are shown in the map. The scenes are labelled after the last five numbers in the file name.

1. Introduction

1.1 Background and objectives

GEUS has been involved in geoscience mapping in Greenland for many years and for many different purposes. Originally, GEUS focused on traditional geological mapping using specialised logistical methods for fieldwork and methodologies to compensate for the arctic environment. Gradually, other geoscience disciplines were involved such as geochemical and geophysical surveys and later remote sensing from aircraft and satellites. The various geographically and geologically different environments encountered in Greenland demanded different combinations of methods, but over the years, it became the standard to use multi-disciplinary approaches involving the full range of techniques. Since the mid-eighties, remote sensing data and methods have been studied, developed and applied by GEUS for regional mineral resource assessments; see Thorning, Thomassen et al. (2019) for an overview.

GEUS now undertakes regional and national mineral resources assessments by carefully applying the optimum combinations of methods for areas under investigation (Salehi 2018, Salehi, Lorenz et al. 2018, Salehi and Thaarup 2018). Geological mapping and mineral exploration in the high Arctic naturally have to deal with the obstacles created by topography, remoteness and harsh climate conditions. Even today, when comparing with other similar areas in the world, large parts of Greenland that are known for excellent potentials for natural resources, including zinc, lead, gold, iron ore, heavy and light rare earth elements, copper and oil, remain largely underexplored. It is, therefore, very important to aim for good areal coverage of surface observation in any geoscience mapping project. In many parts of Greenland, relatively little tundra vegetation and lichen cover provides especially good candidate regions for remote sensing studies.

In the project described here, a set of online available Advanced Spaceborne Thermal Emission and Reflection Radiometer (ASTER) scenes have been collected, compiled, and analysed to obtain geological information for large parts of North East Greenland, prior to field operation in summer 2018. This is important for cost-effective logistics since the geological information extracted from remote sensing satellite data before going into the field, can ensure efficient planning of the fieldwork. Furthermore, the remote sensing data can be brought into play again later, when the ground truth has been established, and the distribution and extent of geological units and formations is interpreted and must be committed to the emerging geological map.

The success of ASTER data for geological purposes has been proven in various regions all over the world (Abdeen, Thurmond et al. 2001, Rowan and Mars 2003, Gomez, Delacourt et al. 2005, Hewson, Cudahy et al. 2005, Di Tommaso and Rubinstein 2007) and ASTER data have been used in all the latest mineral resource assessment projects in West, and South-West Greenland (Salehi 2018). Original plans at GEUS aimed for complete coverage of all ice-free Greenland (still a goal), and the present results from North

East Greenland demonstrate the usefulness of such an undertaking. Although some adaption of standard processing is necessary to properly handle data from the Arctic environment, the cost-effective and straightforward approaches applied in this project are good solutions for reconnaissance stages of mineral exploration in logistically difficult parts of the high Arctic environment. As intended, the achieved results can serve as fundamental building blocks for geological mapping and resource evaluation.
The following overall objectives have been determining the course of the project:

1. The acquisition, quality control and basic processing of 124 ASTER scenes from North East Greenland. Three of these scenes were used for a pilot study focused on the MMR fieldwork area for 2018.
2. The choice of processing procedures and the selection of the ASTER indices best suited for Arctic environments. The processing was supplemented with special processing routines and methods developed by GEUS.
3. The availability of results and maps prior to the 2018 MMR fieldwork; harvesting of ground truth where possible.
4. The delivery of maps and inclusion of maps in the Greenland Web-Portal[1].

[1] http://data.geus.dk/geusmap/?mapname=greenland_portal

2. Geological setting

The geology of North-East Greenland is dominated by the N–S-orientated Caledonian Fold Belt formed by the collision between Laurentia and Baltica 465–400 million years ago. The Caledonian orogeny is characterized by abundant granitic intrusions and westwards transportation of large thrust sheets. After the orogenesis, coast-parallel rift basins formed during the Upper Palaeozoic and Mesozoic. This was terminated by Tertiary uplift and magmatism (Higgins, Gilotti et al. 2008).

In the focus area, 73°45´ to 76°00´ N. latitude, the Caledonides comprise three main units: a Palaeoproterozoic crystalline gneiss-granite basement, a Mesoproterozoic high-grade metasedimentary unit (Krummedal supracrustal sequence) and a slightly deformed and metamorphosed Neoproterozoic-Lower Palaeozoic sedimentary sequence. The 900–600 Ma old basal part of this sequence constitutes the Eleonore Bay Supergroup, a 14–16 km thick unit of marine siliciclastic and carbonate sediments intruded by Caledonian granites (Sønderholm and Tirsgaard 1993)

During the extensional collapse of the Caledonian orogeny, an up to 8 km thick pile of Devonian continental clastic sediments and minor volcanics were deposited in N–S-orientated basins in central East Greenland (Larsen, Olsen et al. 2008). The Devonian basins are bounded by a western fault zone and the so-called Post-Devonian Main Fault. The latter is a regional N–S-trending brittle structure characterized by abundant hydrothermal alteration and sulphide mineralisation (Harpøth 1986). After initial rifting in the earliest Carboniferous, a more than 3 km thick sequence of fluvial sandstones and shales were deposited in narrow N–S-trending half-grabens. The Upper Permian siliciclastic and carbonate sediments in central East Greenland represent the first marine transgression after the Caledonian orogenesis. They are overlain by shallow and deep-water sandstones and shales deposited during continuous rifting in the Triassic, Jurassic and Cretaceous. The extensive Palaeogene plateau basalts on Hold with Hope and Wollaston Forland, as well as basaltic sills and dykes in the Mesozoic sediments, belong to the East Greenland Tertiary volcanic province (Henriksen 2009).

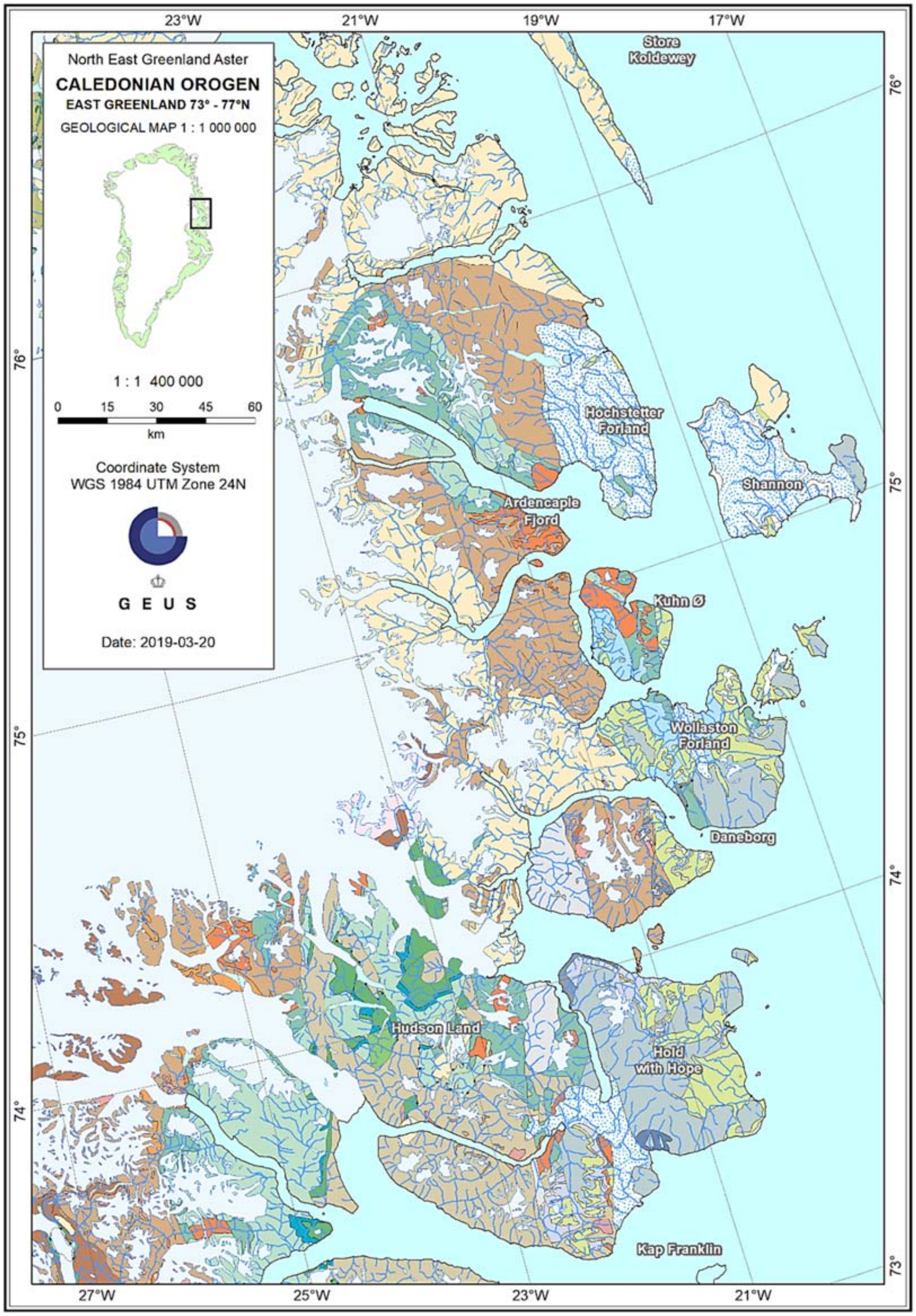

Figure 2. Geological map of North East Greenland in 1:1 000 000 scale (Henriksen 1997, Escher 2001). See geological legend in Figure 3.

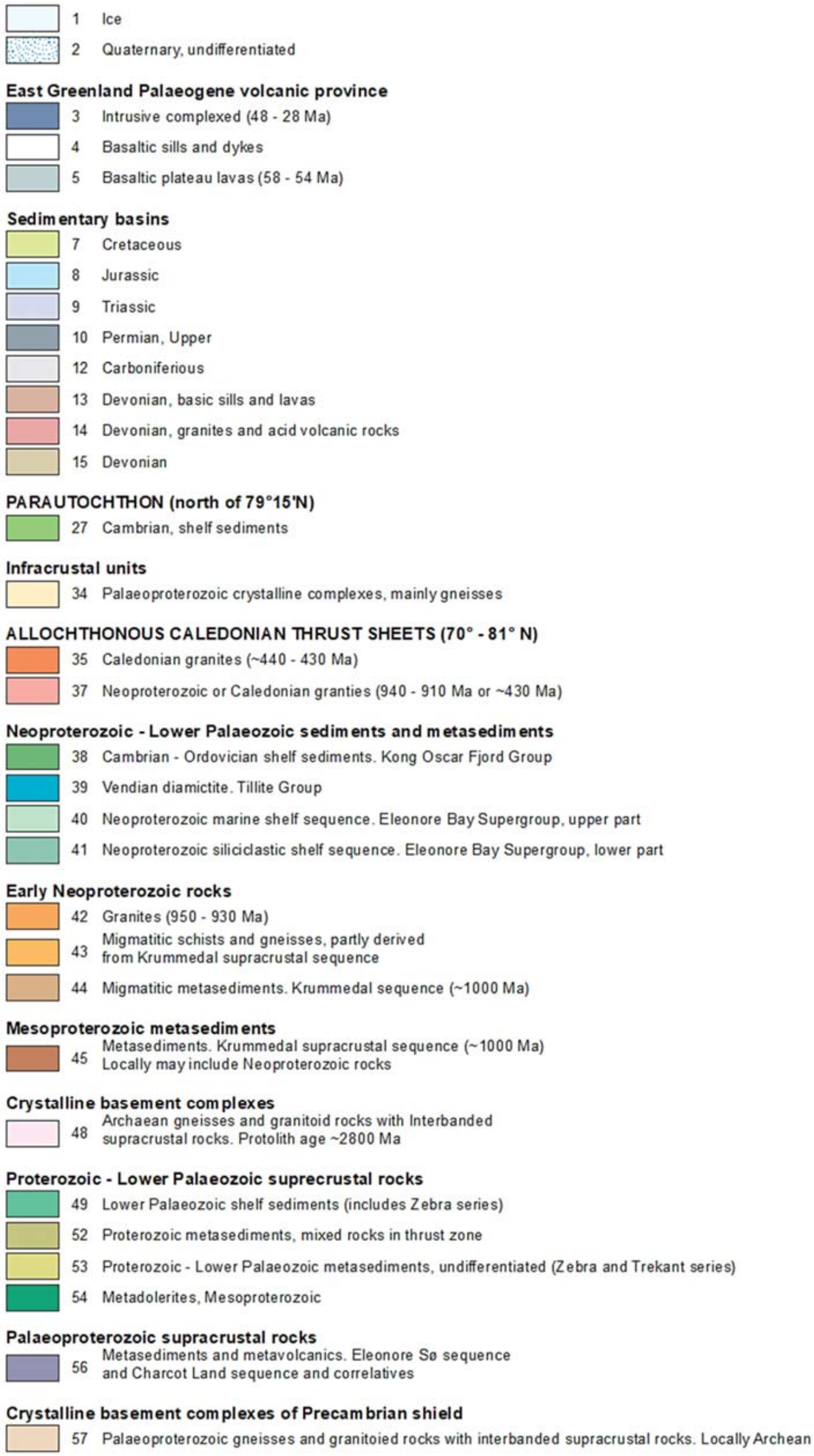

Figure 3. Legend to the geological map in Figure 2.

3. Materials and methods

3.1 ASTER data and characteristics

ASTER is a multispectral instrument on board of the National Aeronautics and Space Administration (NASA) Earth Observatory System (EOS) launched in December 1999. The instrument consists of three subsystems measuring the reflected and emitted radiation in 14 spectral bands i.e. three bands in the visible and near-infrared (VNIR), six bands in the shortwave Infrared (SWIR) and five bands in the thermal infrared (TIR) wavelength regions; with spatial resolution of 15, 30, and 90 meters, respectively (Figure 4).

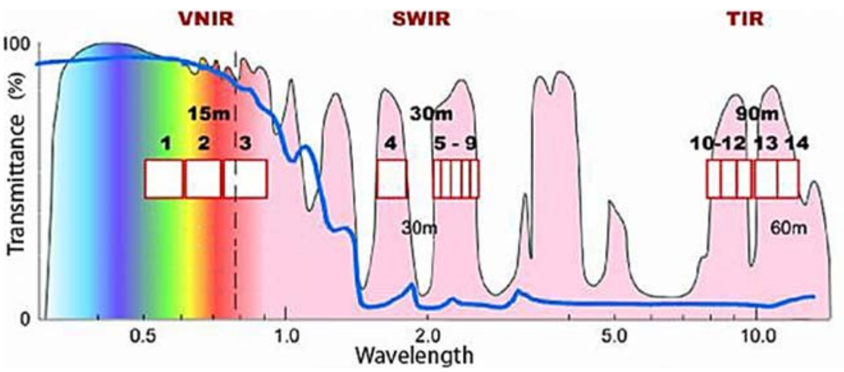

Figure 4. Location of ASTER spectral bands in the atmospheric transmission spectrum (Wahi, Taj-eddine et al. 2013)

Despite the broad bandwidth of the ASTER bands, the instrument is useful for mapping alteration patterns or specific mineral assemblages known to be associated with mineral systems. The VNIR and SWIR wavelength regions can provide mineralogical information for exploration purposes based on analysis of electronic absorption features in transitional metals (Fe^{2+} and Fe^{3+}), absorption bands due to SO bending overtones and of molecular absorption features in carbonate (CO_3), hydrate (H_2O) and hydroxide (OH) minerals (Hunt 1977). Band 1 and band 3 are mainly suitable for detecting Fe-oxides; band 5 and band 6 for detecting Al–OH absorption features in clay minerals, alunite and/or muscovite/sericite; band 7 mainly for detecting Fe–OH features in jarosite and/or Fe-muscovite and band 8 for detecting Mg–OH features related to chlorite, epidote and/or carbonates (CO_3). The five bands of the TIR subsystem are most useful for mapping primary rock-forming silicate minerals and their related impurities within surficial deposits. It is important to remember that ASTER generally provides spectral signatures of mineral groups rather than specific minerals (Hewson, Cudahy et al. 2005, Hewson, Robson et al. 2015). For example, using ASTER data it is not possible to differentiate between different types of carbonates such as calcite and dolomite. The overall shape of the spectrum can sometimes be used to map minerals with similar spectral characteristics. For example, the presence of the ferrous iron spectral ramp between 0.8 and 1.6 μm can be used to distinguish MgOH minerals chlorite and talc (Figure 5).

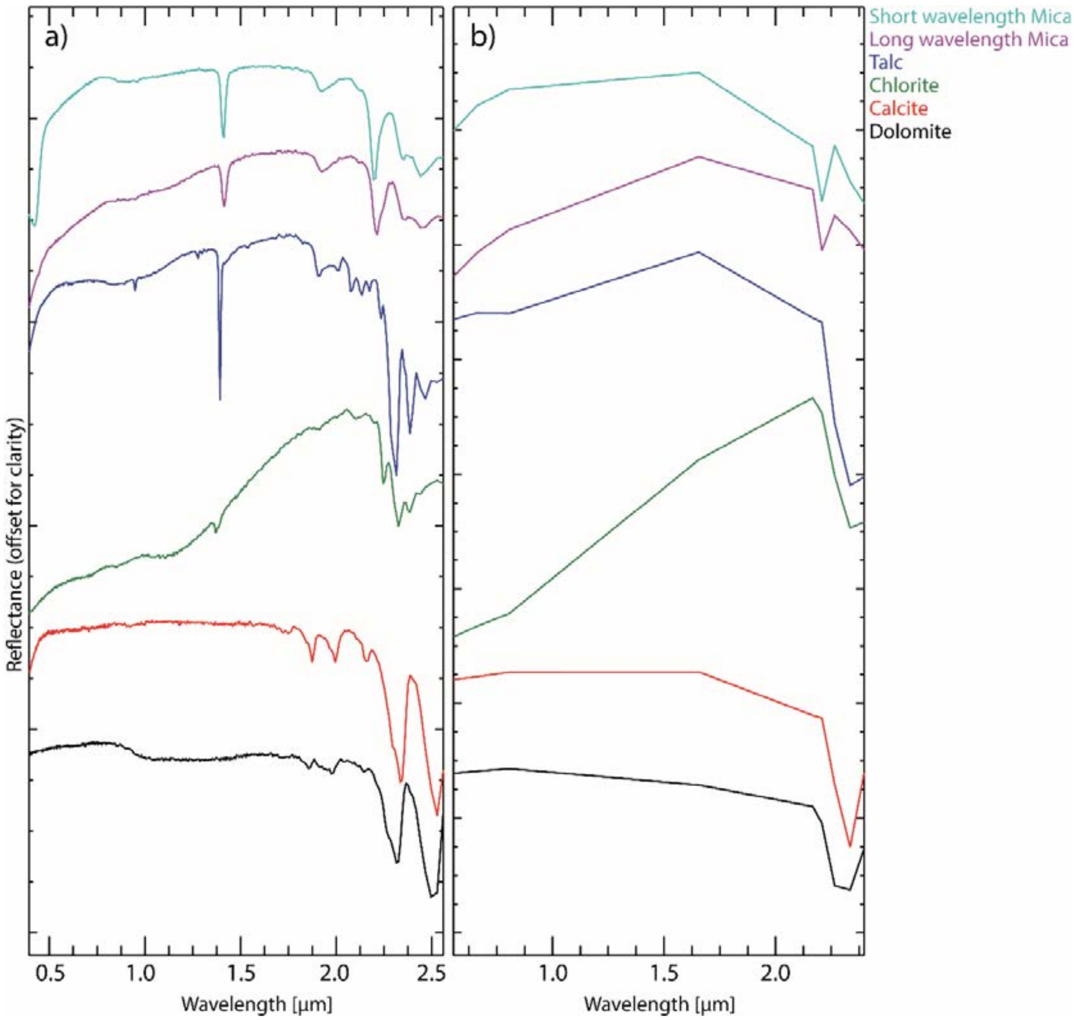

Figure 5. (a) Standard spectra from the USGS library in the VNIR and SWIR from mica, talc, chlorite, calcite, dolomite (Clark, Swayze et al. 2007) given at laboratory spectral resolution and (b) resampled at ASTER bands

3.2 Digital Elevation Model[2] and Topographic Map[3]

As partner of this project, ASIAQ provided a Digital Elevation Model for North East Greenland (Figure 6). The input data used for generating this elevation map is obtained from the ArcticDEM project (PGC 2017), which uses Digital Globe WorldView-1, WorldView-2 and WorldView-3 raster DEM strip files. The data have a spatial resolution of 8-meter pixel size and are referenced to the WGS84 ellipsoid. The DEM data are recorded from 2012 to 2015. Several steps are needed for selection of data strips prior to generating the mosaic:

1. Best mutual match in z values for overlapping strips (DEM-differencing)
2. Low degree of bad or partly corrupted data

[2] Contact person: Mikkel Høeg Bojesen; Phone: +299 348871; E-mail mhb@asiaq.gl
[3] Contact person: Christian Brogaard Pedersen; Phone: +45 91333961: E-mail: cbp@geus.dk

3. Date of recording, giving preference to ice free summer months June-August, though acceptable images exist from April, May and September as well
4. Low Nadir angle was preferred over large Nadir angle

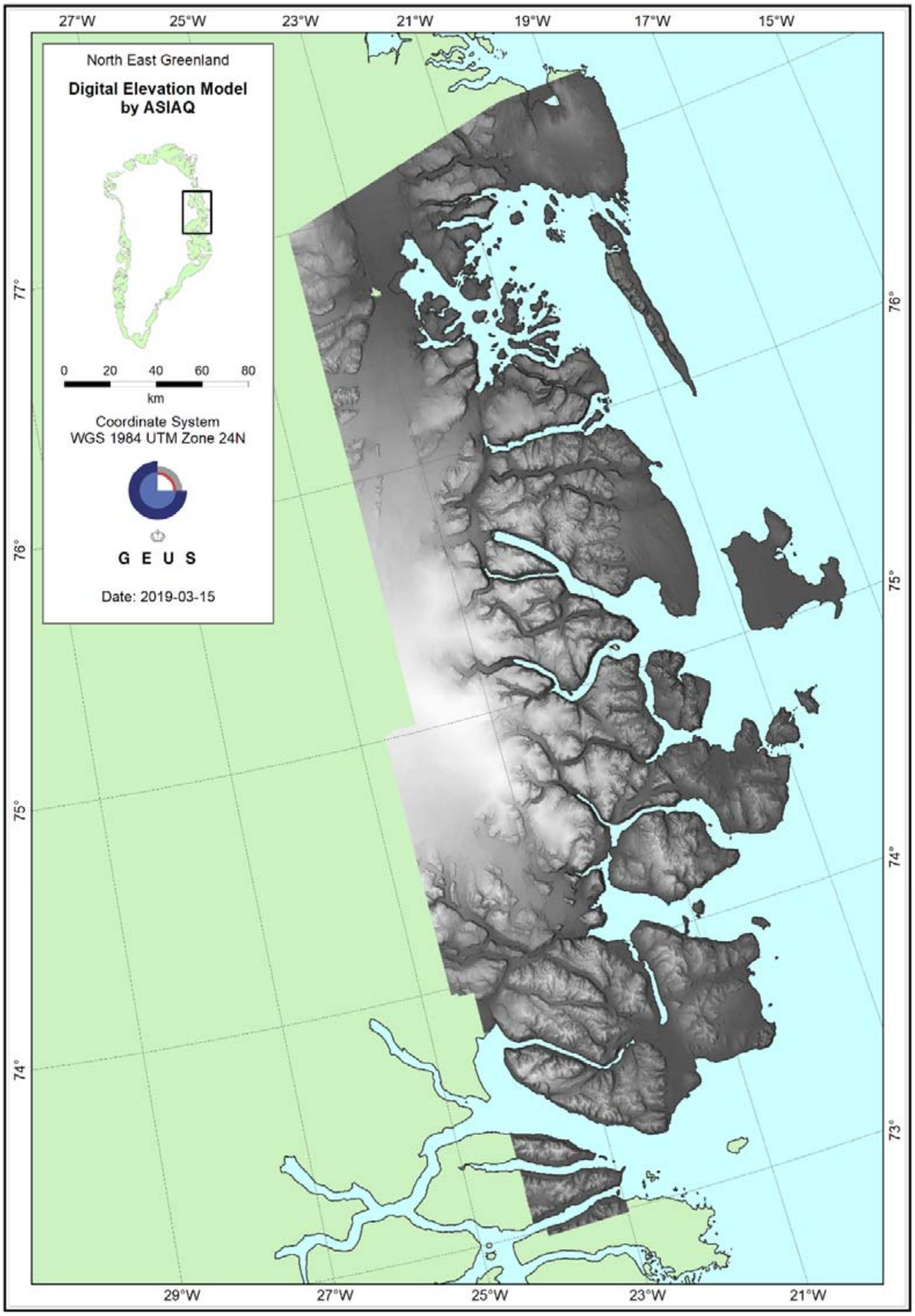

Figure 6. The Digital Elevation Model from North East Greenland provided by ASIAQ.

Not all input data strips from the ArcticDEM came with uniquely suggested shifts xyz-wise, with respect to IceSAT. A workflow for co-registration of all included DEM strips is established without the use of reference data. The co-registration is carried out using the OPALS software (opalsGeoref package), in which least square matching of overlapping elevation information is used to obtain optimal shifts for all DEM strip files included. Seamless mosaicking is carried out with ENVI 5.4 by applying a median filter (3x3 kernel size).

The elevation map was provided in a GeoTiff file format and is re-projected to WGS 84 UTM Zone 24 North (EPSG 32624) and imported to an ESRI file geodatabase. The topographic map (TM) of Northeastern Greenland (Figure 7) is then generated based on the elevation map delivered by ASIAQ.

Figure 7. The topographic map generated within the project area.

Using ArcGIS Image Analyst, a multi-directional shaded image is created from the elevation map and contour lines are generated with a 10-meter interval. A customized algorithmic color ramp has been produced to give a balanced colorization of the terrain. The final topographic map is then displayed using a bilinear interpolation and symbolized with a custom-made 100-meter interval color legend (Figure 7). Names and other geographical information are taken from GEUS owned database for topographic maps of Greenland in a scale of 1:100 000. It includes riverbeds, lakes and lakes on ice, rivers, ice margins, ice sheets and shorelines. All symbolizing and colorizing of the topographic features are specially made for this particular map. The final map is then hosted as a Web Map Tile Service (WMTS) on GEUS' ArcGIS Image Server and presented on the official Greenland Web-Portal[4].

3.3 Pre-processing of Aster data

ASTER Level 1 Precision Terrain Corrected Registered At-Sensor Radiance (AST_L1T) data is downloaded from the USGS webpage https://earthexplorer.usgs.gov/ between the years 1999 and 2007. Summer day-time acquisitions are chosen as optimal datasets for further processing. Subsequent pre-processing of the data encompasses atmospheric, radiometric and topographic corrections before masking non-outcrop pixels and generating the final mosaic.

The calibrated radiance data are converted to apparent surface reflectance using the radiative transfer program "Atmospheric and Topographic Correction" (ATCOR-3) in the rugged terrain mode. The ATCOR rugged terrain mode utilizes a surface elevation model, here the DEM that has been provided by ASIAQ, to adjust illumination levels. Calibrating and adjusting the apparent surface reflectance values obtained from the ATCOR-3 processing was not possible due to lack of ground-based reflectance measurements. The processing provides a 15-band output '*atm.bsq', where bands 1 - 9 are surface reflectance, bands 10-14 are surface radiance, and band 15 is the surface temperature (the scale factors are included in the '*_atm.hdr'). In addition, an emissivity file (for bands 10-14) is generated.

Features associated with clouds, ice, snow, ocean, lakes and the edges of the image (Figure 8) need to be masked prior to applying any mapping approach. Removal of these unwanted features improves the visualization of slight differences between spectrally similar minerals when applying band ratio or PCA approaches. In particular, abundant vegetation cover can obscure the spectral signatures of the underlying geological substrate and thus lead to poor classification results. In this project vegetation is not masked out from the scenes, but instead an NDVI index is applied to highlight localities with higher vegetation abundances that should be taken into account prior to interpretation of the results.

[4] http://data.geus.dk/geusmap/?mapname=greenland_portal&lang=en#baslay=baseMapGl&optlay=&etent=390535.4662399024,8116399.771731951,1619372.5337600976,8728258.228268048&layers=northpole_graticule,asiaq_dem_east_grl

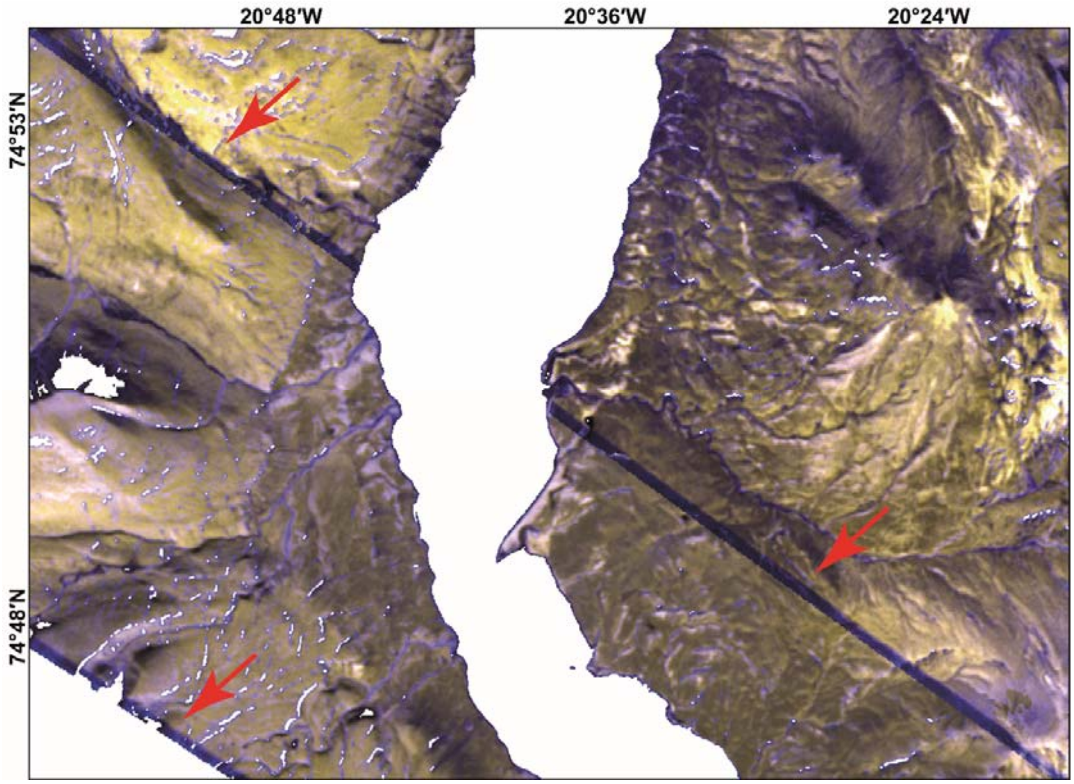

Figure 8. Two ASTER scenes that were merged before masking the image edges. The different bands of ASTER look at a slightly different parts of the Earth's surface. This should be corrected for by ASTERS band-to-band co-registration. However, this process causes artefacts at the edges of color composite images (see purple lines in the image), since some of the bands contain zero (or NaN) and other bands have real pixel values. Therefore, all pixels where any of the bands has no real pixel values should be masked out after layer stacking.

3.4 Image processing techniques

There are a few aspects to be considered when using ASTER data for regional-scale mineral or lithological mapping. Firstly, cloud cover, vegetation and atmospheric effects can severely bias the surface reflectance recorded by the sensor. The impact of such features should be corrected and encountered for prior to performing any mapping approach. Secondly, band ratios do not indicate the occurrence of a mineral with absolute certainty. Results have more a qualitative than a quantitative character such that ground truthing is essential. Because no ground truth was available for validating the results, calibration of used parameters will be the scope of future projects. Thirdly, every terrain is different, so band ratios which work in some areas for a particular mineral or assemblage may not show the same thing elsewhere. Therefore, it is important to consider ASTER images in combination with other data. Datasets such as geological maps, geochemistry, ground spectral measurements, and any other available data should be used in conjunction with ASTER data for the most accurate interpretation.

For calculation of band ratios in TIR wavelength region, radiance is used as opposed to emissivity data. The advantage is that this approach enables analyzing the data acquired at different dates and with potentially very different surface temperatures as one seamless compositional dataset and allows performing decorrelation stretches on the entire dataset for identifying and discriminating compositional units.

3.4.1 PCA images

To decrease the redundant information in highly correlated bands, principal component analysis (PCA) (Gasmi, Gomez et al. 2016) has been applied to the nine VNIR-SWIR ASTER bands. The results of PCA allow validating lithological boundaries in the published geological map, and give new information to identify lithological units that were previously undiscovered.

3.4.2 MNF images

The Minimum Noise Fraction (MNF) transformation is similar to PCA transformation and is applied to VNIR-SWIR ASTER surface reflectance data to assess the spatial variability of different lithologies. MNF transform involves two cascaded PCA transformations (Green, Berman et al. 1988). The first transformation de-correlates and rescales the noise in the data based on an estimated noise covariance matrix. The noise-reduced data is then fed to a standard PCA transformation in the second step. The final outputs are uncorrelated and are arranged in terms of decreasing information content.
MNF components with eigenvalues less than 1.0 are usually excluded from the data in order to improve the subsequent spectral processing results (Jensen 2015). In this study, all eigenvalues of the transformed ASTER data were greater than 1.0, although the actual values clearly decrease with increasing component number. Consequently, all the VNIR-SWIR bands of the ASTER data were retained for subsequent data processing.

3.4.3 Band ratio analysis

Twenty-two classes of rocks and minerals were mapped over an approximately 80.000 km^2 region (Figure 1) using the nine reflectance bands (VNIR-SWIR) and the five radiance bands (TIR) of ASTER. Targeted rocks and minerals include:

(1) carbonate rocks containing either abundant calcite, dolomite mixtures, argillaceous and (or) weathered carbonate rocks containing residual clay minerals
(2) clay mineral deposits of a variety of origins containing either mixtures of or abundant amounts of kaolinite, illite, smectite and (or) muscovite or phengite
(3) quartz rich rocks and siliceous rocks
(4) ferricrete, gossan, laterite

Other materials that are abundant enough and have uniquely strong spectral signatures are detected based on specific band ratios and by using two or more ASTER bands (Rowan, Hook et al. 2003, Rowan and Mars 2003, Rowan, Mars et al. 2005).

3.4.4 Band ratio combination

Band ratio combination has been proven to be one of the most efficient measures for lithological discrimination in the past (Gad and Kusky 2006, Amer, Kusky et al. 2010, Pournamdari, Hashim et al. 2014). A total of 13 combinations (see Appendix 2) were performed in this project to examine which combinations are the most suited and relevant for the geological settings of North East Greenland. From the 13 combinations, three were identified as the most suitable;

1) Combining the band ratios 4/7, 4/3 and 2/1
2) Combining the band ratios 4/1, 3/1 and 12/14
3) Combining the band ratios 4/2, 4/5 and 5/6.

These combinations enhanced the spectral differences of relevant lithological units such that they can be distinguished easily.

4. Results and discussion

4.1 PCA

The response of each component of the principal component analysis has been compared to the geological map (see Figure 2). The second component of PCA seems to contain more lithological information than other components. The eighth and ninth components are noisy and seem to contain no relevant lithological information. Principal component bands with large eigenvalues and the largest amounts of data variance were employed to give the best discrimination between the various lithological units (Figure 9).

By means of the second, third and sixth principal components of the PCA, the main geological groups (Quaternary rocks, Palaeogene basalts and intrusions, Palaeoproterozoic crystalline complexes, Neoproterozoic-Lower Palaeozoic sedimentary sequence and Mesoproterozoic metasediments) are distinguishable (compare Figures 2 and 9). Quaternary rocks are less characterized by defined lithologic units but are more associated with a mixture of unconsolidated rocks accumulated by glacial and fluvial processes. These rocks are clearly visible as pixels with cyan colors in Figure 9. The PCA exhibits contrasted responses inside Palaeogene, Palaeoproterozoic, Neoproterozoic-Lower Palaeozoic and Mesoproterozoic groups. This can be explained by a larger variety of different specific lithologies and rock types present in those groups.

Indeed, this PCA transformed data contain important information about geology, topography, and surface roughness. The geological information is easier to extract from principal components than from initial ASTER data. Some units appear poorly identified due to their limited outcropping size or the existence of strong slopes. Despite of these limitations, the generated images of the PCA have potential to improve the existing geological map. Deviations between lithological boundaries in current geological maps and principal component analysis results can be employed by geologists to revise and upgrade the geological maps. For example, magenta pixels in Figure 9 (around center part of Shannon Ø) are not outlined in the geological map. Other magenta pixels in north and southern boundaries of this island correspond with mafic dykes and sills in 1:500 000 scale geological map (Escher 2001). Considering the shape of these pixels that cut through the center part of the island, we suggest that they can be related to intrusions (mafic dykes and sills).

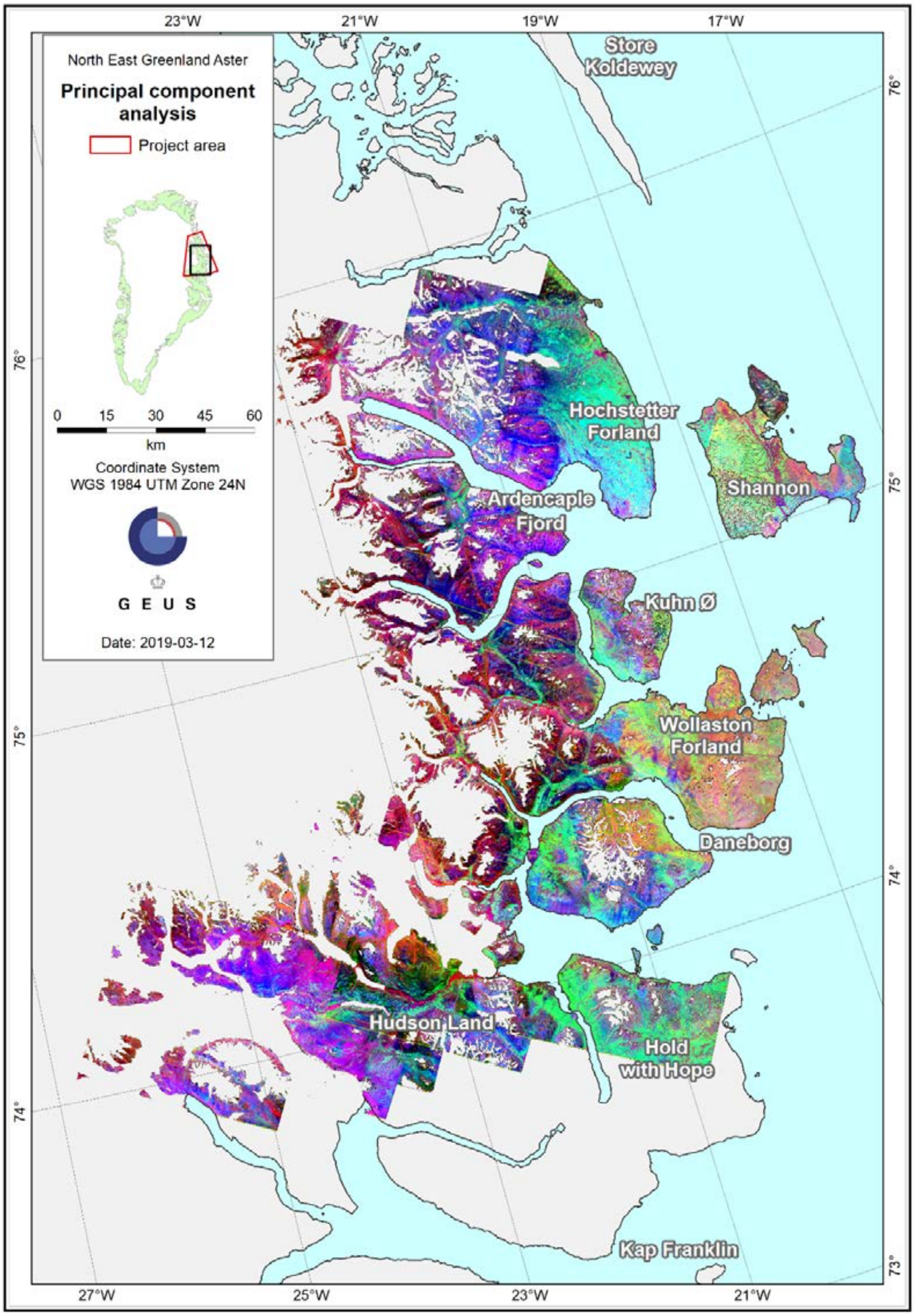

Figure 9. ASTER PCA false color composite (Red: PC2, Green: PC3, Blue: PC6)

4.2 MNF

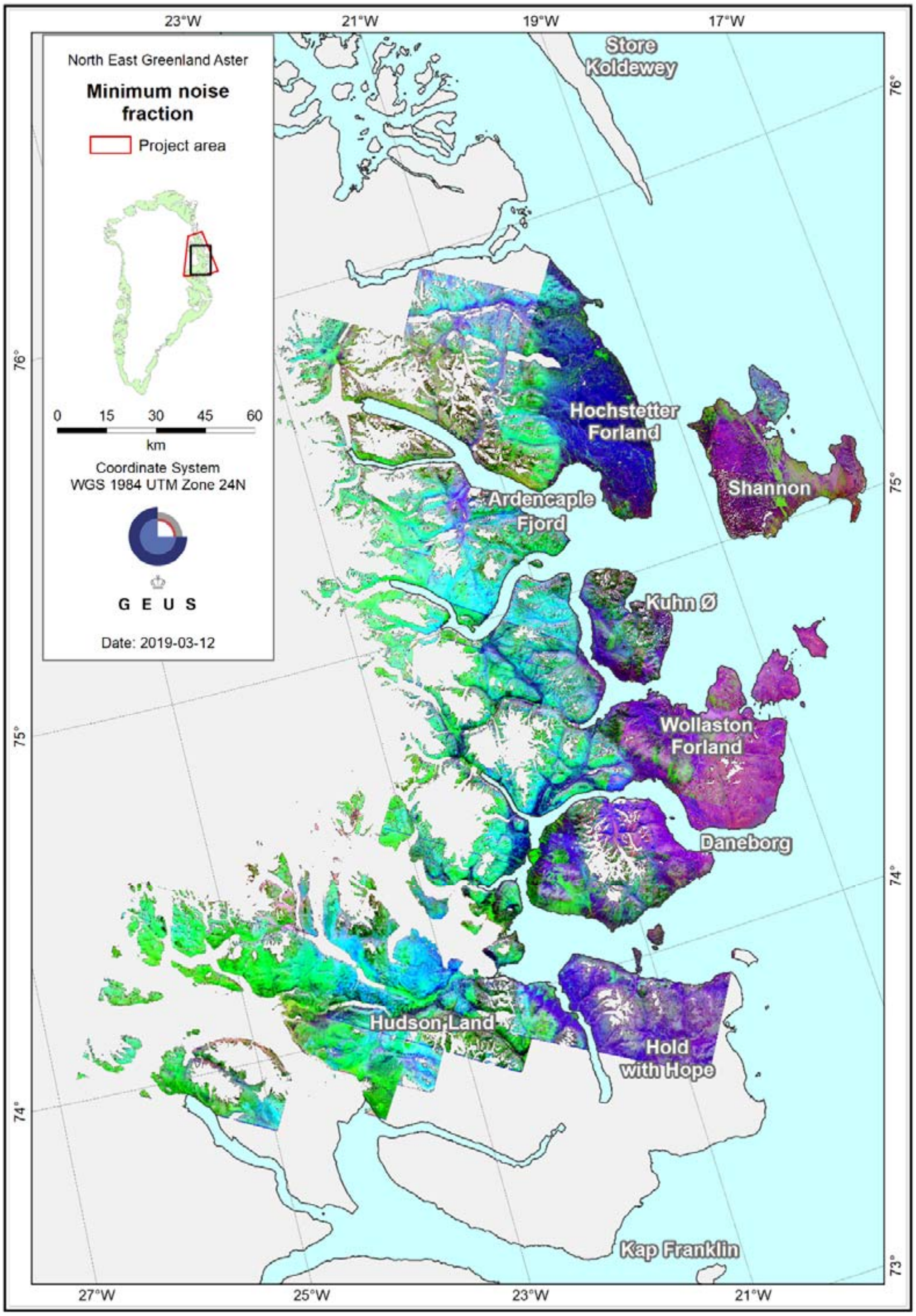

Figure 10. ASTER MNF false color composite (Red: MNF1, Green: MNF2, Blue: MNF4)

The lithological map derived from MNF transform shows strong agreement with the published geological map (compare Figures 2 and 10). The boundaries between different types of lithologies are better demarcated in MNF color composite image as compared to PCA color composite image (see Figures 9 and 10). Quaternary rocks are represented by dark blue colored zones in the MNF color composite image. Migmatitic metasediments (Krummedal sequence) correlate with green-cyan shaded pixels (e.g. in Hochstetter Forland, Thomas Thomsen Land). Late Proterozoic sandstones and siltstones (unit number 41 in geological map) match well with olive-green colored zones. Pink colored zones in Wollaston Forland are associated with Basaltic Plateau Lavas in the geological map. Some lithological features that are present in the MNF color composite image are not described by any specific unit in the geological map as for example, the green trend on the Shannon Ø and Wollaston Forland.

4.3 Band ratios

4.3.1 Iron feature

4.3.1.1 Ferric iron, Fe3+

Ferric-iron (Fe3+) rich rocks exhibit a sharp decline in reflectance approximately from 0.8 µm towards shorter wavelengths. Thus ferric-iron rich exposures are associated with very high ASTER 2/1 band ratio values. Red-color areas in the map (Figure 11) indicate rocks with higher iron content.

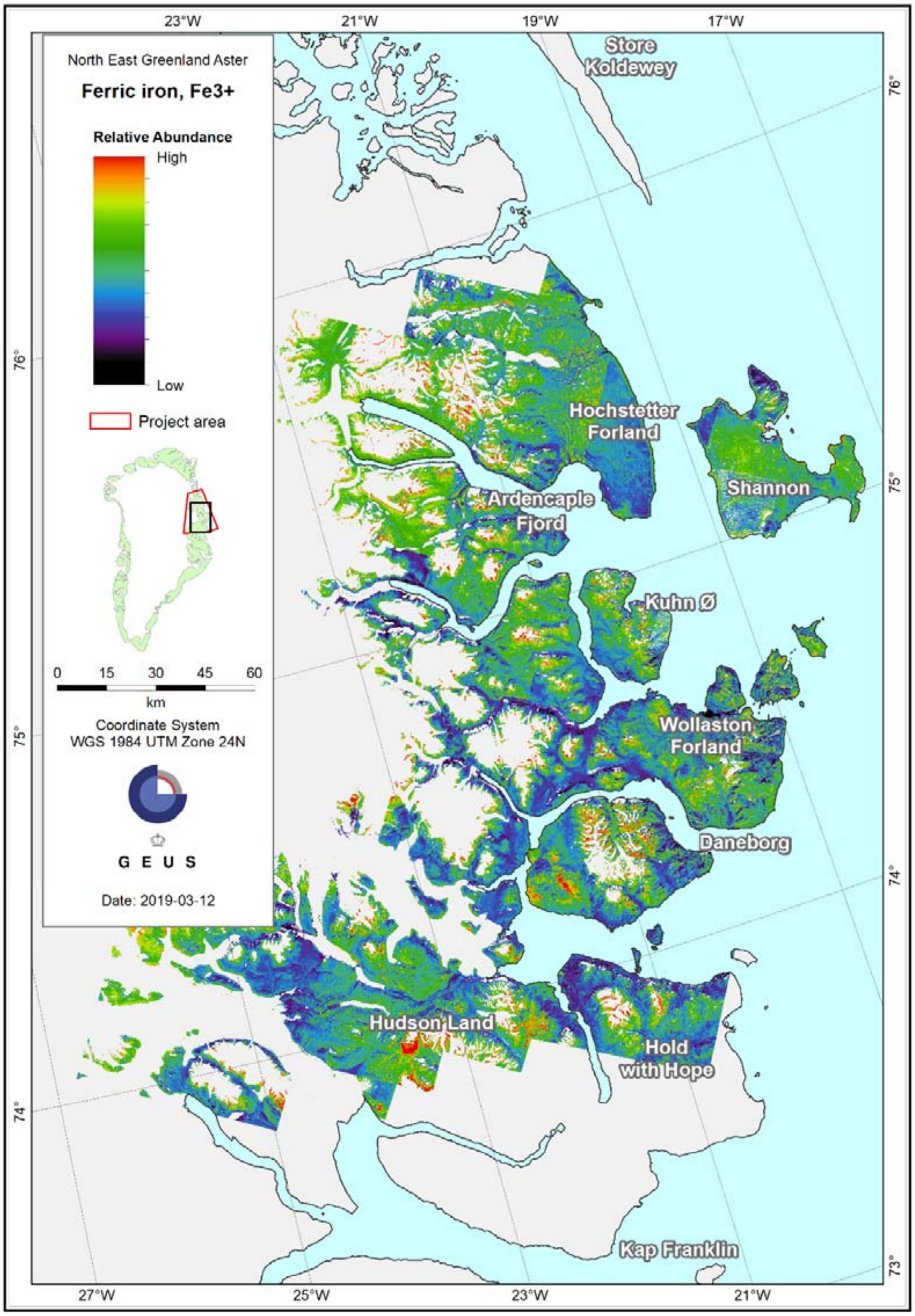

Figure 11. Ferric iron abundance map (B2/B1)

4.3.1.2 Ferrous silicates (biotite, chlorite, amphibole)

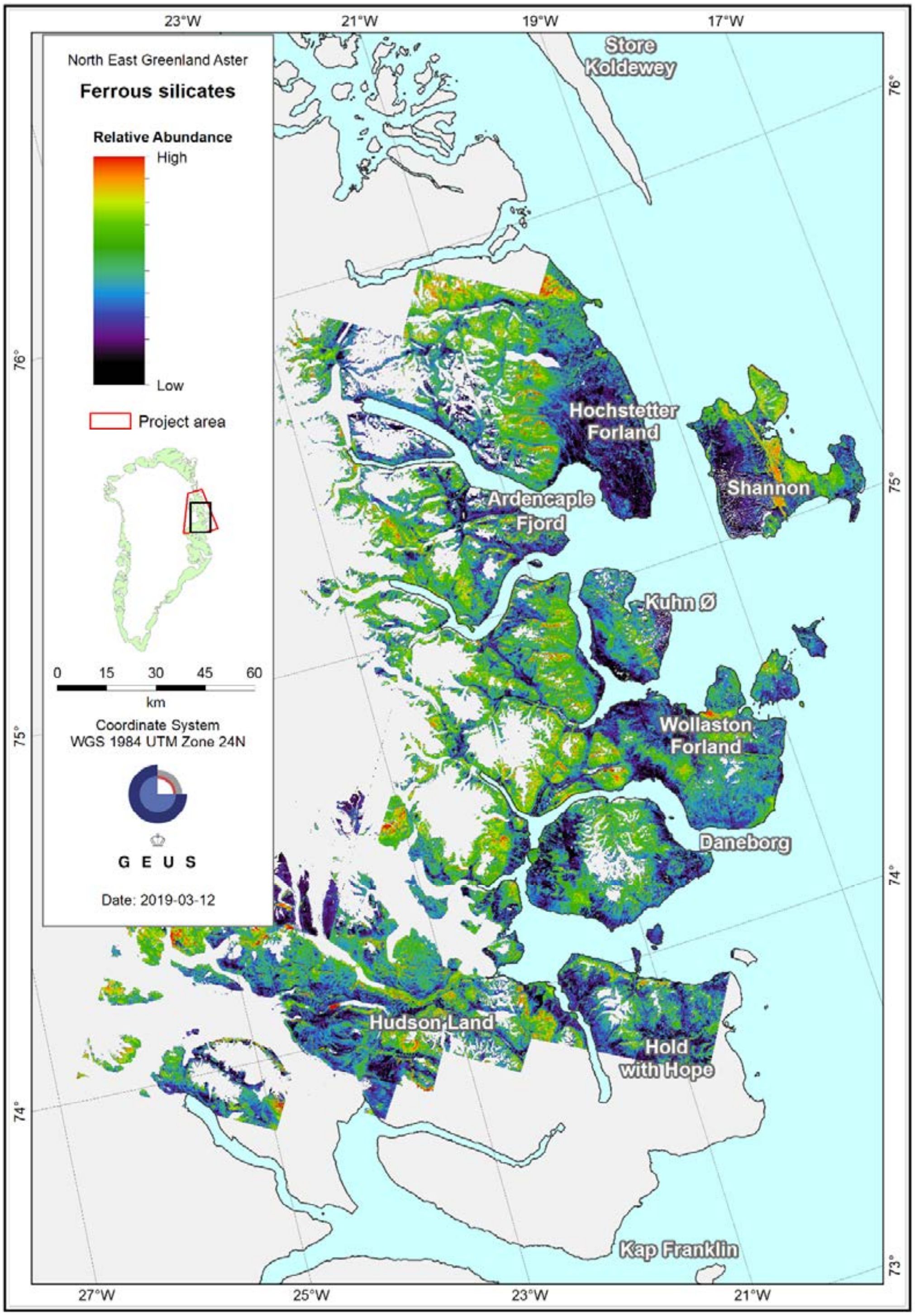

Figure 12. Ferrous silicates abundance map (B5/B4)

Quaternary rocks have dark image signatures on 5/4 band ratio image (Figure 12). This is probably due to the spectral reflectance curve of clays and/or vegetation that exhibit lower reflectance values around 2.1 µm (band 5) as opposed to 1.6 µm (band 4), which leads to small ratio values associated with dark colors. There are some areas with high ferrous silicate ratio values in Shannon Ø and Wollaston Forland (Figure 12) that correlate with mafic dykes and sills (mainly dolerites) in the geological map (Figure 2). Medium band ratio values correlate well with regions associated with migmatitic metasediments and orthogneiss in the geological map.

4.3.1.3 Ferric oxides

Iron oxide minerals zones are typically associated with reddish color altered rocks. These minerals, which include hematite, goethite, limonite and jarosite have a reflectance peak in the visible red (0.7 µm) and absorption feature near 0.9 µm and 0.4 µm.

The iron oxide abundance map has been generated using bands three and four in order to highlight the iron oxide bearing minerals. This index map highlights all the materials having red color. This includes iron ores, red soils, rust, laterites etc.

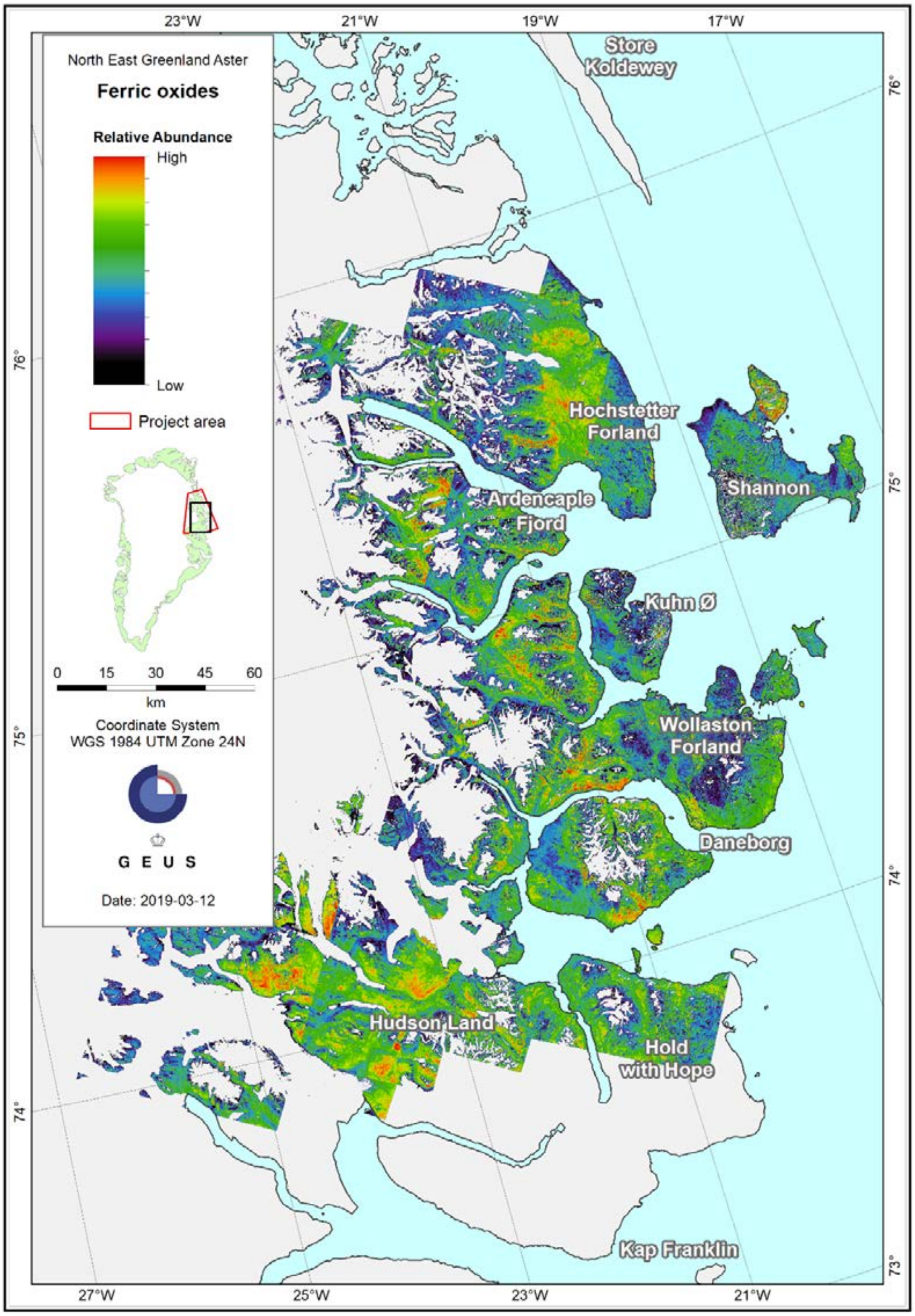

Figure 13. Ferric oxides abundance map (B4/B3)

4.3.2 Carbonates/mafic minerals

Relative abundances of MgOH (e.g. present in chlorite, hornblende and carbonate group minerals) were estimated based on their 2.33 µm (band 8) absorption feature and their reflectance values at the shoulders (bands 7 and 9). Such an index map can be used to distinguish metamorphic rocks and different varieties of metavolcanics.

4.3.2.1 Epidote / chlorite /amphibole

High values of this index indicate areas that are associated with an enrichment in carbonate, epidote, chlorite, and amphibole minerals (see red and orange colors in Figure 14, highlighting limestones and dolomitic limestones in Hudson land). Siliciclastic sediments have lower contents of these minerals and are shown with very dark blue colors in Figure 14. In addition, it can be applied to distinguish the metamorphic rocks and the different varieties of metavolcanics.

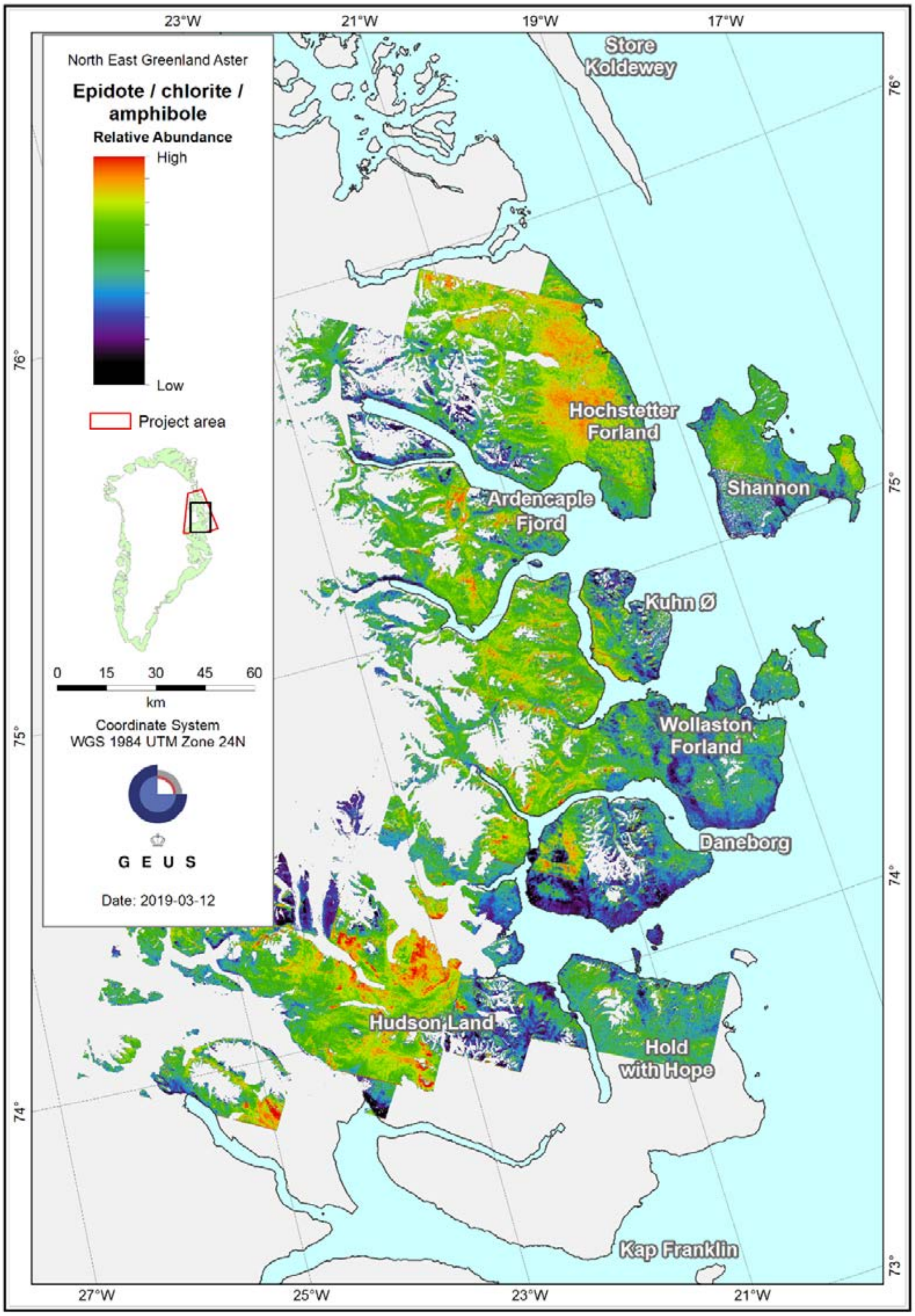

Figure 14. Epidote / chlorite / amphibole abundance map (B6+B9/B7+B8)

4.3.3 Silicates

ASTER SWIR spectra of AlOH minerals (e.g., kaolinite, Al-poor and Al-rich mica) indicate changes in the symmetry of the AlOH absorption feature centered at 2.2 µm (band 6). Duke (1994) has shown that the chemistry of white mica (e.g., muscovite/illite, phengite) and particularly its Al content has an impact on the wavelength of this absorption feature. According to this study, Al poor micas (e.g., phengite) display a AlOH absorption feature at a longer wavelength than Al-rich micas. On basis of this behavior , an estimate of AlOH abundance can be obtained by using a (5+7)/6 band ratio, and white mica composition can be inferred from the 5/6, 7/6 and 7/5 band ratios.

4.3.3.1 Sericite / muscovite /illite / smectite

High values in the abundance map (Figure 15) mainly correlate with sedimentary rocks in the geological map (Figure 2). The dark areas in the band ratio image (e.g. eastern part of Hochstetter Forland) are probably related to vegetation coverage and the low reflectance values of vegetation within the the bands 5, 6 and 7. Therefore, the band ratios may not indicate the occurrence of a mineral with high reliability and overlapping spectral features of other materials within an individual pixel can alter the final spectral response.

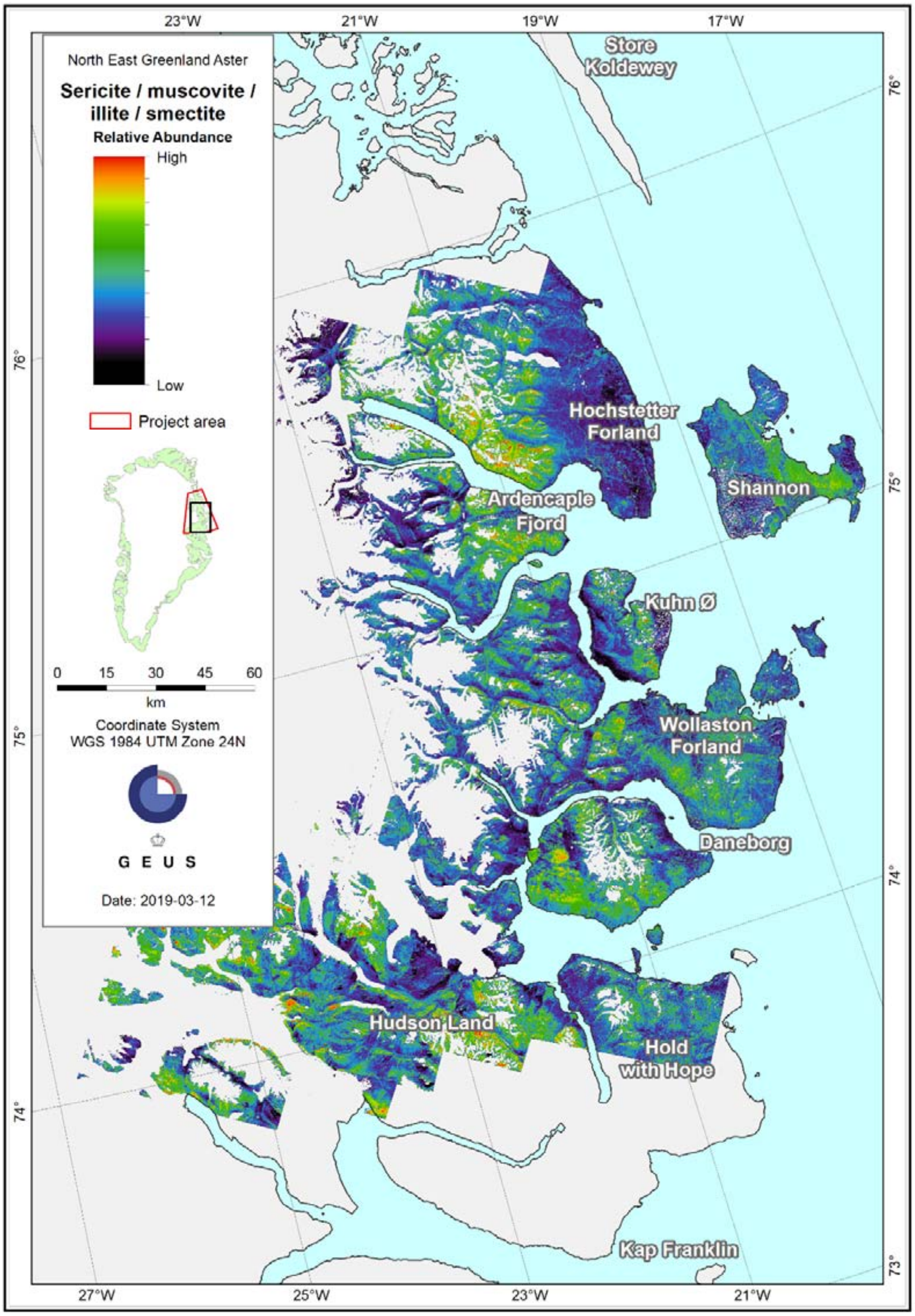

Figure 15. Sericite / muscovite / illite / smectite abundance map (B5+B7)/B6

4.3.3.2 Alunite / kaolinite /pyrophyllite

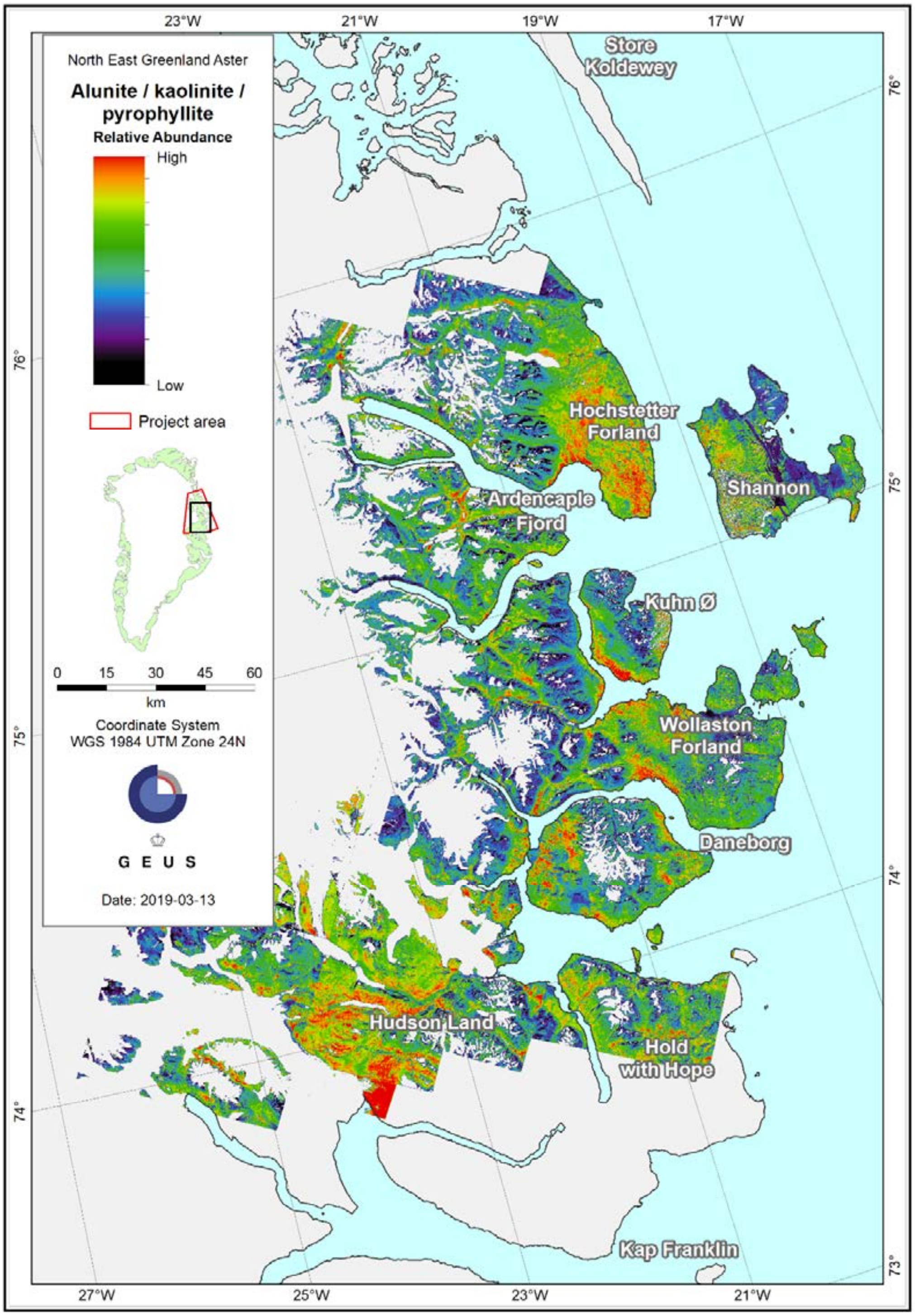

Figure 16. Alunite / kaolinite / pyrophyllite abundance map (B4+B6)/B5

OH-bearing minerals, mainly kaolinite, alunite and montmorillonite, are characterized by an absorption feature in band 6 resulting in lower reflectance in band 6 compared to the bands 4 and 7. Kaolinite has an additional low absorption feature in band 5, whereas alunite has absorption features in both band 5 and 8. The ASTER (4+6)/5 band ratio provides a hydrothermal alteration indicator for areas, where it is likely to find alunite, kaolinite, pyrophyllite and illite (Testa, Villanueva et al. 2018).

4.3.3.3 Phengitic

Some of the high values correspond with quaternary overburden in the geological map. This can be false positives due to clay minerals that have an absorption feature around 2.2 µm. Dark, grey-green to brownish weathering, alternating units of quarzitic sandstone, banded sandstone and mudstone, black, silty mudstone and occasional calcareous intercalations in the area (e.g. in Kuhn Ø) show up with dark values in the band ratio image (Figure 17). Mafic dykes and sills will also show up with dark colors (e.g. in Shannon Ø) due to their low phengitic band ratio values (peak in reflectance around band 6).

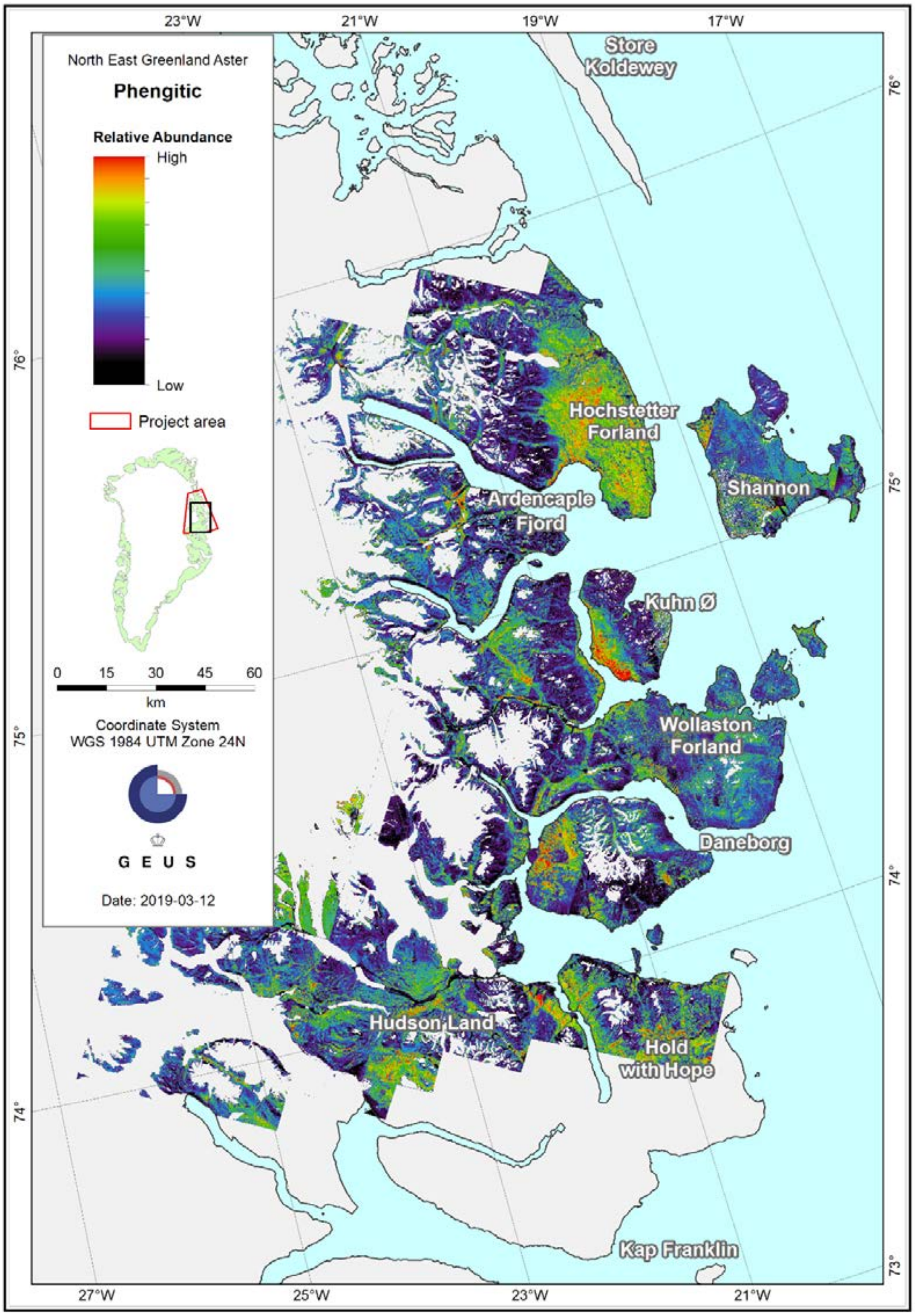

Figure 17. Phengitic abundance map (B5/B6)

4.3.3.4 Muscovite

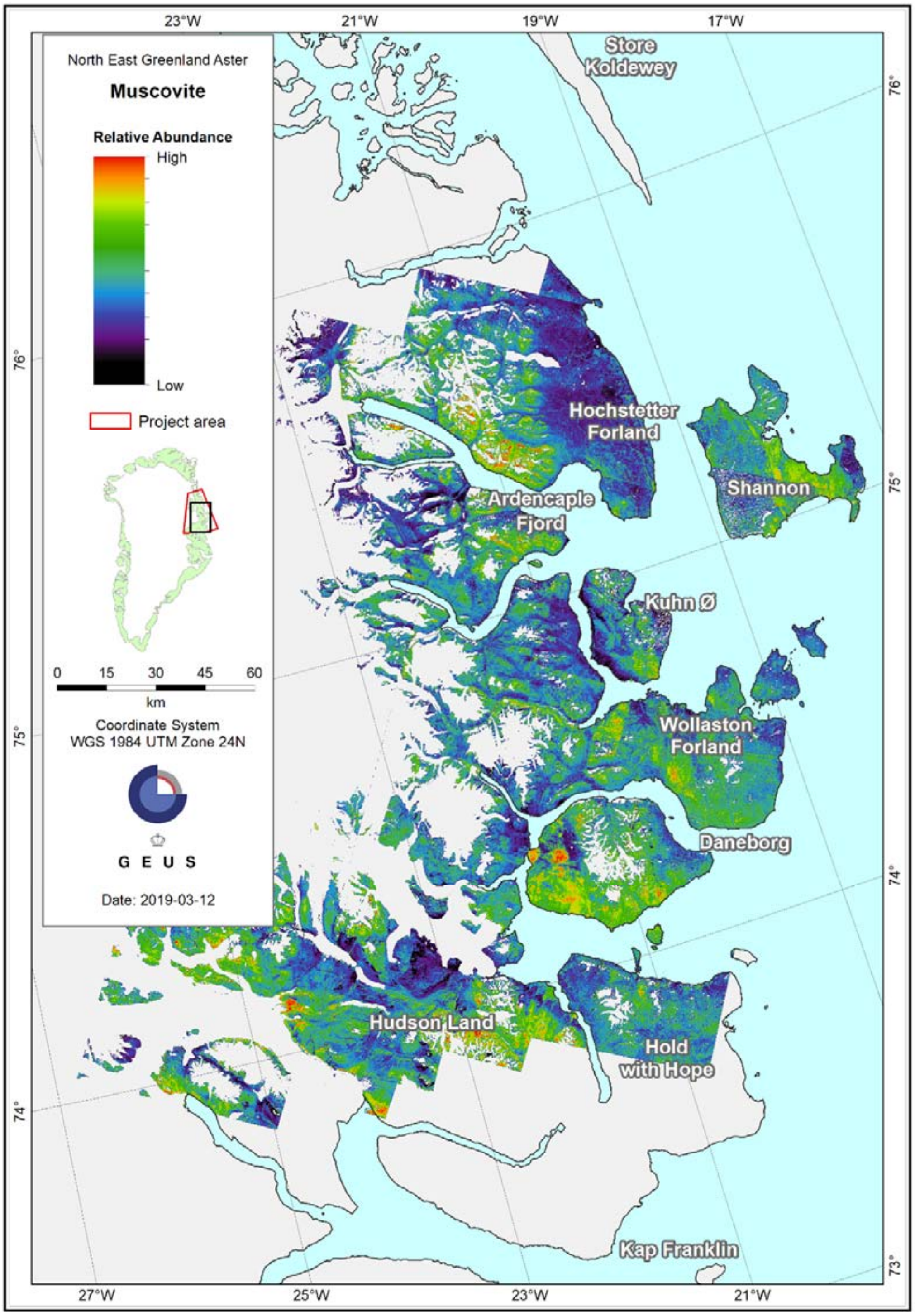

Figure 18. Muscovite abundance map (B7/B6)

Lower Plateau Lava Series in Hold with Hope, Wollaston Forland, Kuhn Ø and Shannon show up with dark pixels in the band ratio image (Figure 18). According to the literature (Upton and Emeleus 1977, Watt 1994, Larsen, Pedersen et al. 2014), this geological unit is mostly aphyric quartz tholeiites. High values sometimes coincide with metasediments and granites in the geological map.

4.3.3.5 Kaolinite

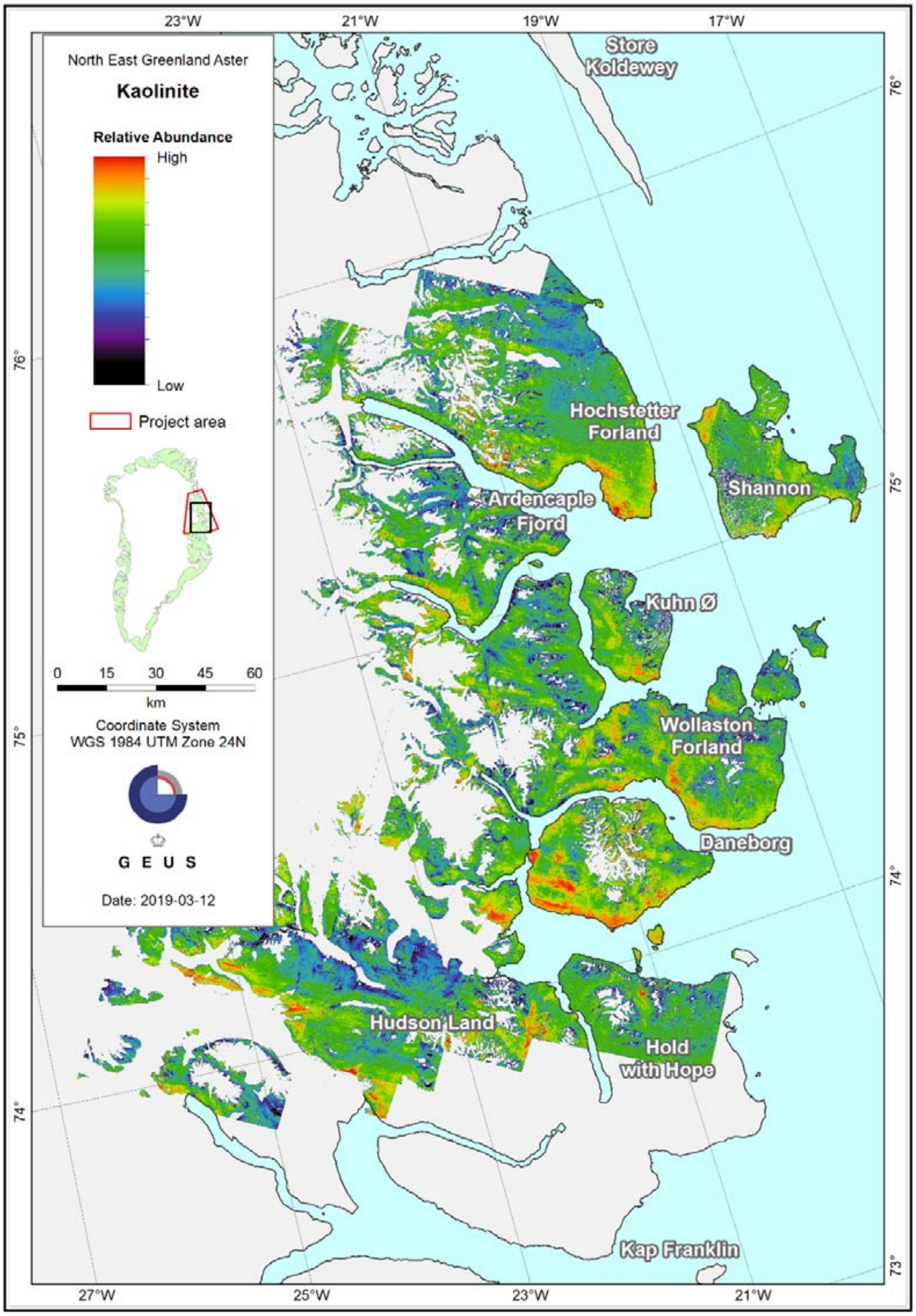

Figure 19. Kaolinite abundance map (B7/B5)

Kaolinite has characteristic absorption features at band 5 (2.145–2.185 µm) and band 6 (2.185–2.225 µm) but only the last absorption is diagnostic for mica group minerals. Although some of the medium to high value pixels in the scene could be a response to the presence of kaolinite, others could be due to muscovite – illite.
Jarosite has a strong absorption feature in band 7 (2.235–2.285 µm), where kaolinite has a diagnostic reflection such that presence of jarosite very likely does not cause any interference.

4.3.3.6 Alteration

ASTER bands are highly sensitive to alteration minerals (Bierwirth 2002, Volesky, Stern et al. 2003). For example, VNIR bands are well-suited to detect Iron oxides. Band 4 of the SWIR is affected by argillic alteration, band 6 by propylitic alteration and the bands 4, 5 and 8 by phyllic alteration.
AlOH minerals such as kaolinite, muscovite, montmorilonite and illite (major minerals for phyllic and argillic alteration zones) have the highest reflection in band 4 in the

SWIR. But Mg-OH minerals such as chlorite and epidote that are indicative for propylitic alteration zones have the strongest reflection in Band 5 and 6 in the SWIR.

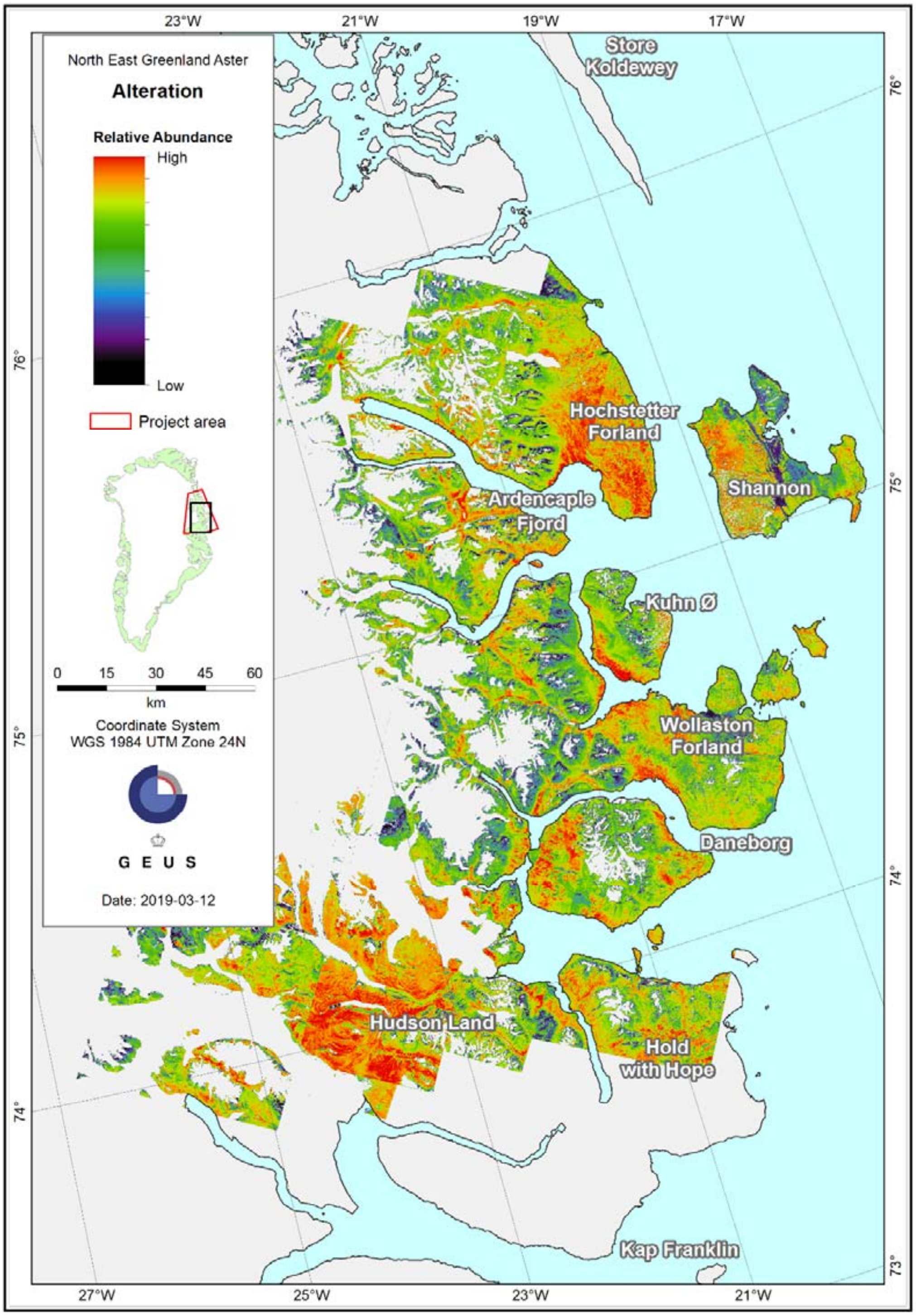

Figure 20. Alteration abundance map (B4/B5)

4.3.4 Silica

4.3.4.1 Siliceous rocks

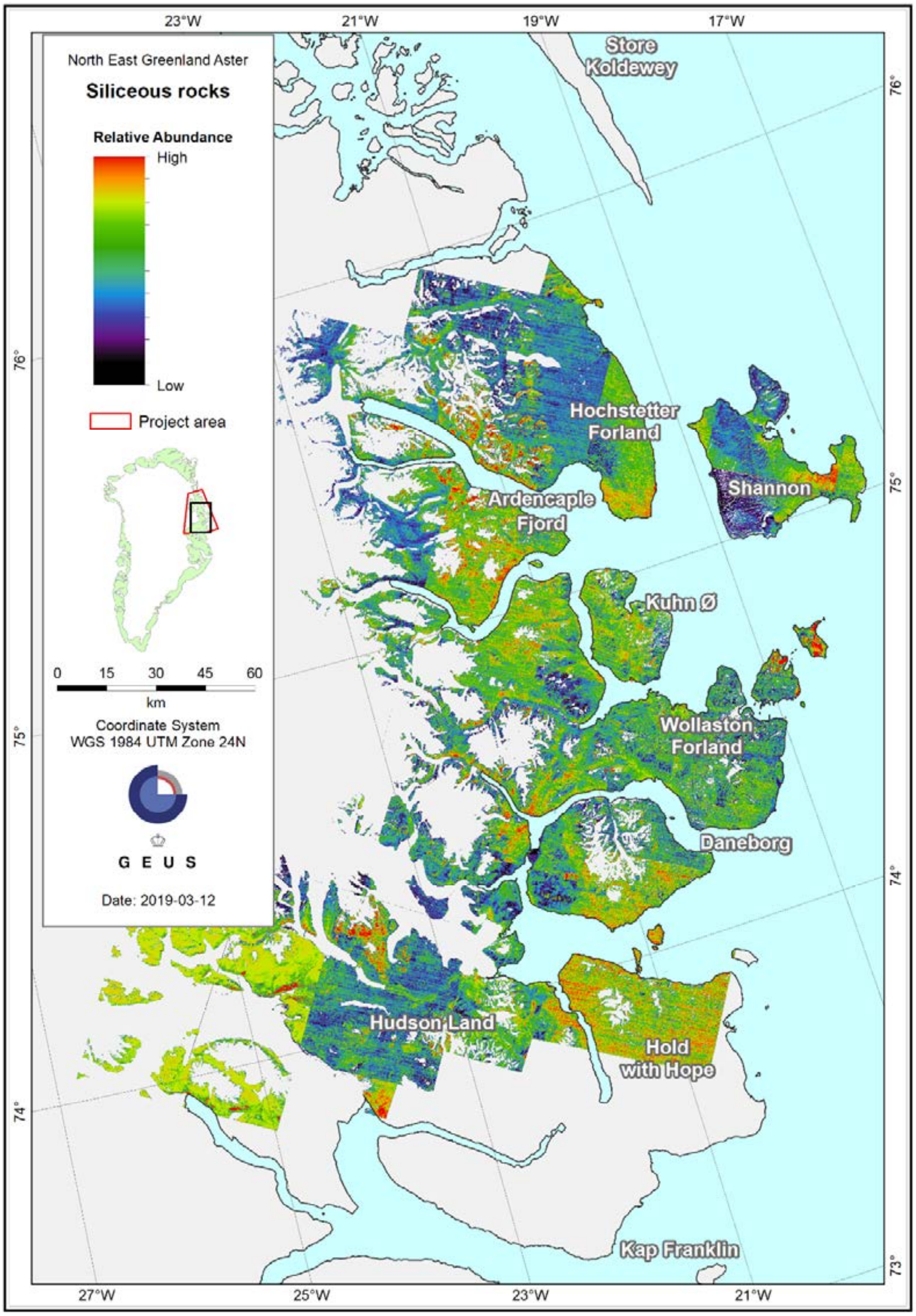

Figure 21. Siliceous rocks abundance map (B11xB11)/(B10xB12)

The thermal infrared bands (8-12 μm) are very useful in mapping lithologies and distinguishing between rock-forming mineral groups like silicates and carbonates and for mapping lithologies that lack VNIR-SWIR absorption features. For example, siliceous rocks can be mapped using SiO_2 absorption features in TIR data, whilst mapping these rocks using the VNIR-SWIR data is not possible, because quartz VNIR-SWIR spectra are featureless in this range.
The red areas in the siliceous rocks index map (Figure 21) correspond to Eleonore Bay Supergroup in Ole Rømer Land and Hudson Land (see geological map), which is described as alternating units of white to purple weathering products, fine to medium grained sandstone, and dark green, brownish or dark red, silty mudstone and heterolithic mudstone (Tirsgaard and Sønderholm 1997). High values are also observed for migmatitic metasediments in Clavering Ø and Thomas Thomsen Land that were derived by partial melting and for Lower Plateau Lava Series, which are mostly aphyric quartz tholeiites.

4.3.5 Others

4.3.5.1 NDVI

The Normalized Difference Vegetation Index is a measure of the chlorophyll content and, hence, plant growth. This measure has been used with ASTER imagery for a long time. The index is a ratio of NIR+RED / NIR-RED. Color range of the resultant NDVI image is stretched to enhance its contrast. This index can be very useful in assessing vegetation stress variations related to e.g. the underlying rock formations or water availability. Red tones in the NDVI index map indicate higher abundances of vegetation.

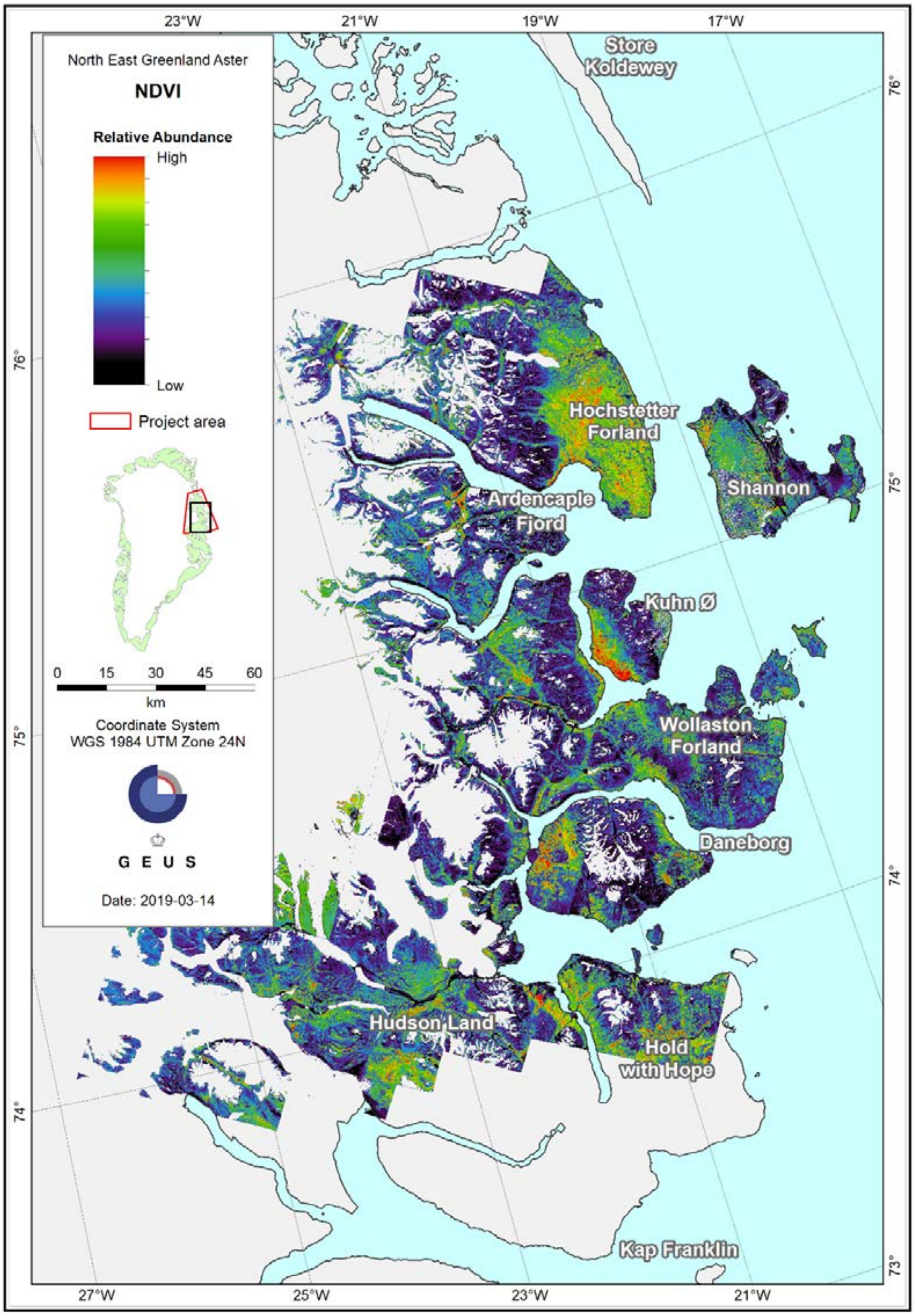

Figure 22. NDVI abundance map (B3-B2)/(B3+B2)

4.4 Band ratio combination

Generating false-color composite images from ASTER band combinations (Figure 27) or band ratio combinations (Figure 23-26) can reveal important mineralogical\lithological information. Here, we generate false color composite images using VNIR and SWIR band ratios to separate the main lithological groups exposed in the study area. Each ratio value is displayed in red, green, and blue hues (proportional to their values). As higher the ratio value as more of its color is represented in the pixel. The respective colors for the three ratio values are combined in the color-ratio composite image map (see the index map in Figures 23-26). High values of only one of the ratio values are displayed in hues of its respective primary color. Two ratios with high values are displayed as the combination of their two primary colors. For example in the color composite image for argillic alterations in Figure 23, a pixel with a high 5/6 ratio (phengite) and a high 7/6 ratio (muscovite) is displayed yellow (red + green) if both ratios are of a similar value. If the 5/6 value is higher than the 7/6 value, the pixel will be orange. If the 7/6 is larger than the 5/6, the pixel will be yellowish-green.

4.4.1 AlOH-minerals/advanced argillic alteration

This color composite image (Figure 23) highlights the argillic alteration areas and is based on the compositional nature of the Al-OH mineralogy. High band ratio 5/6 values typically highlight host rocks, high 7/6 values show the presence of muscovite and high 7/5 values highlight presence of kaolinite. According to Hewson, Cudahy et al. (2004), this combination separates minerals with right asymmetric 2.2 μm absorption features like phengite (in red) from ones with symmetric 2.2 μm features like muscovite and illite (in green) and with left asymmetric 2.2 μm features like pyrophyllite, alunite, dickite, and kaolinite (in blue). This change in symmetry is related to the loss of aluminum in the white mica and the substitution of silica, magnesium, or iron. Thus, red to green tones are theoretically related to areas rich in Al-poor to Al-rich white mica, whose absorption features have longer and shorter wavelength, respectively, whereas blue areas show a contribution of kaolinite.

Sedimentary rocks, such as mudstone, shale, claystone and litharenite sandstone, contain large amounts of detrital clays such as montmorillonite, illite and kaolinite; these can be erroneously mapped as hydrothermally altered clay minerals.

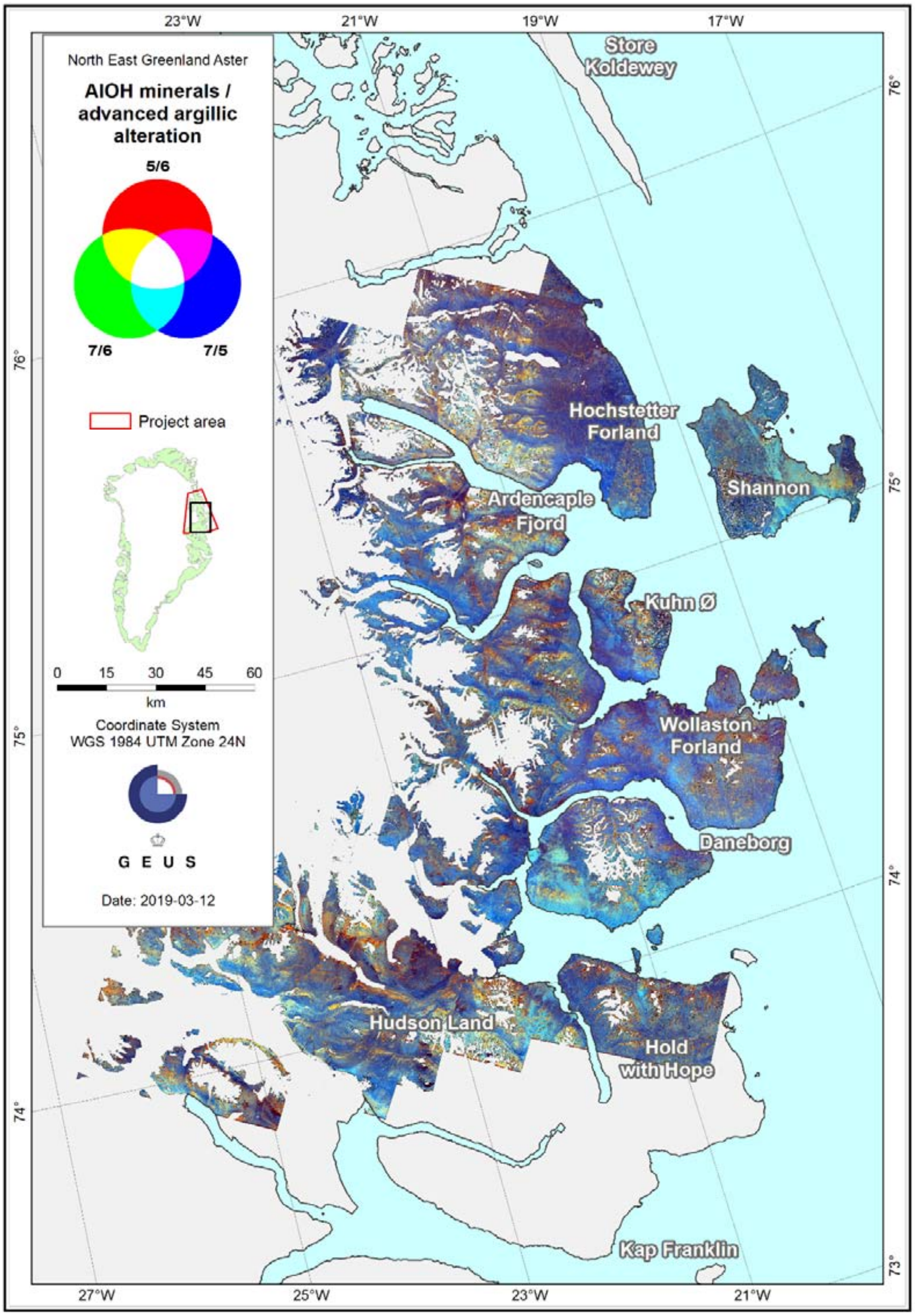

Figure 23. RGB false color composite image of ASTER band ratios, highlighting advanced argillic alterations (Al–OH minerals). Red: B5/B6, Green: B7/B6, Blue: B7/B5

4.4.2 Clay-Amphibole-Laterite

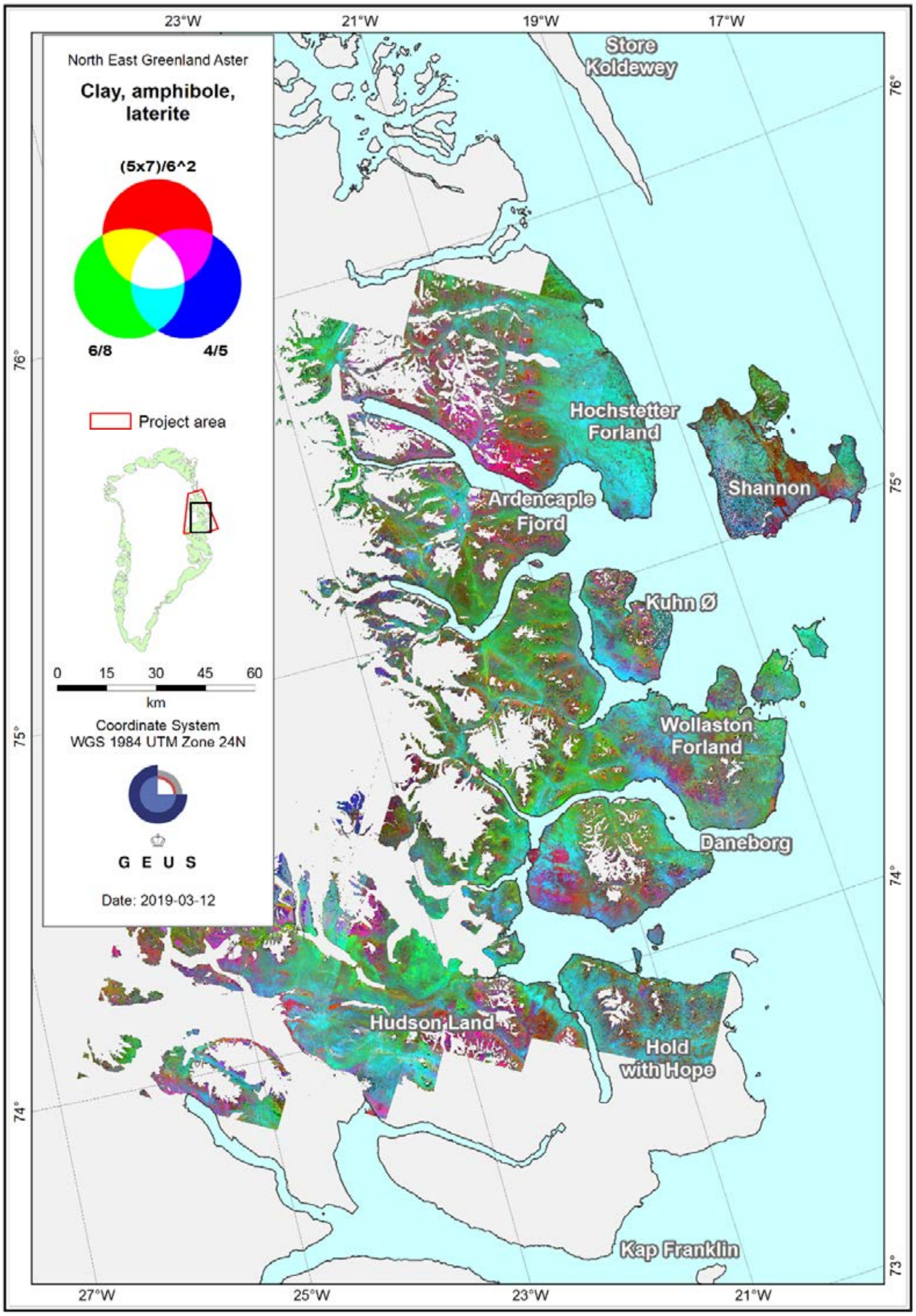

Figure 24. RGB false color composite image of ASTER band ratios, highlighting clay, amphibole and laterite in red, green and blue, respectively. Red: (B5xB)/(B6xB6), Green: B6/B8, Blue: B4/B5

Band ratio combination image that uses the ASTER (5 x 7)/(6 x 6), 6/8, and 4/5 band ratios (Figure 24), highlights clays, amphiboles and lateritic alteration with red, green and blue shades, respectively.
High clay ratio values (red colored pixels) are associated with Proterozoic metasediments (migmatitic pelitic, semi-pelitic and psammitic metasediments). Brownish pixels correspond to Carboniferous-Permian sandstones and shales. Quaternary rocks show high amphibole and laterite ratio values (green and cyan colored pixels).

4.4.3 Gossan, alteration, host rock

ASTER band ratio color combination images can be used for differentiating the alteration zones and gossans from the host rock (Volesky, Stern et al. 2003). This is done by identifying two assemblages of minerals namely, iron minerals and the minerals found in hydrothermally altered rocks, which include calcite, clay, and chlorite-rich zones (Abdelsalam and Stern 1999, Abdelsalam, Stern et al. 2000).
Red areas in the image represent gossan (iron-rich) rocks, which are relatively scattered and localized (Figure 25). Yellow color areas are associated with iron oxide minerals and potential areas of alteration. The host rock has a purple hue in this image (Figure 25).

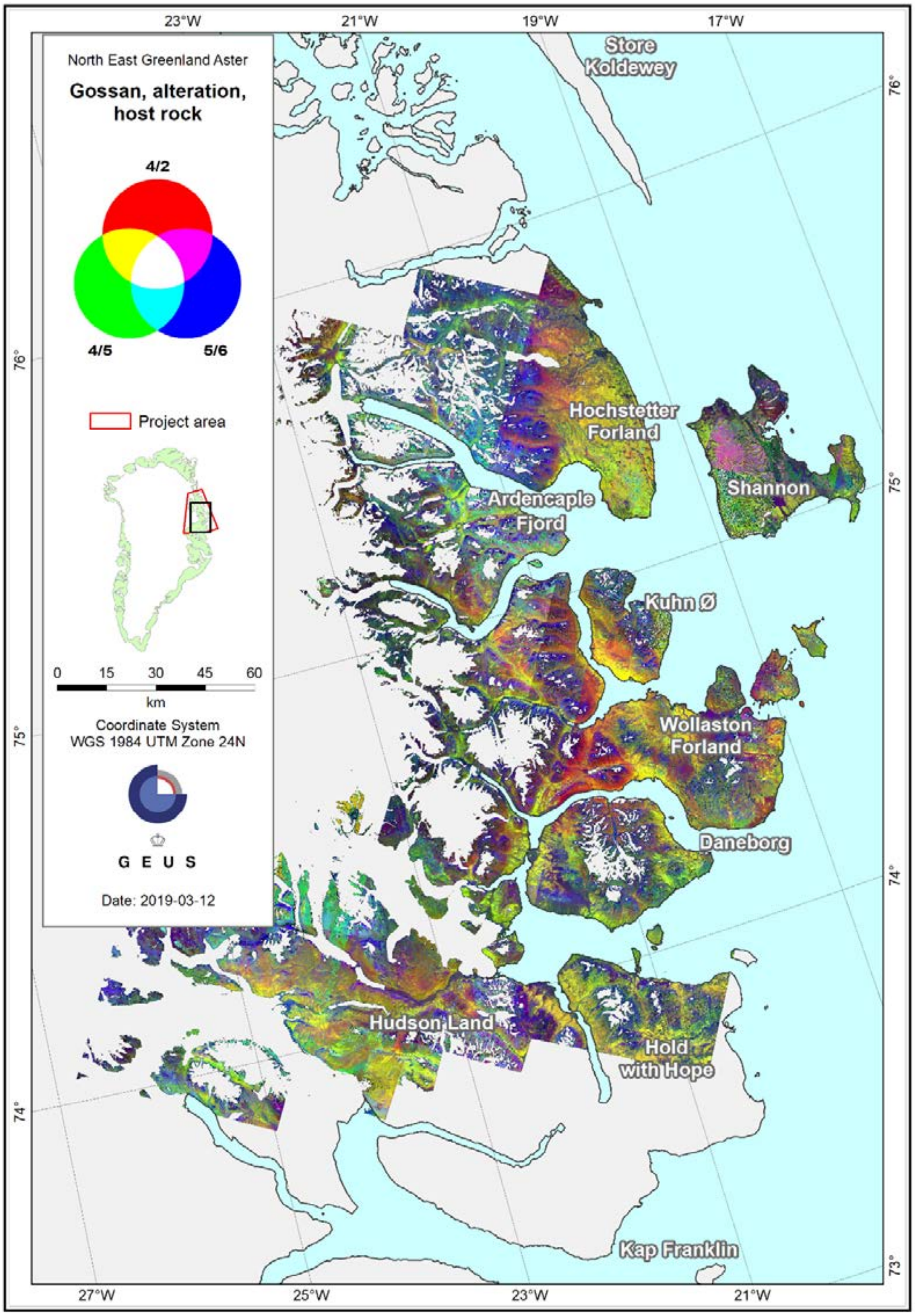

Figure 25. RGB false color composite image of ASTER band ratios, highlighting Gossan, alteration, host rock. Red: B4/B2, Green: B4/B5, Blue: B5/B6

4.4.4 Discrimination

Abdeen, Thurmond et al. (2001) suggested (4/7, 4/1, 2/3 x 4/3) and (4/7, 3/4, 2/1) band ratio colour combination for mapping serpentinite, granite and marble lithologic units of the Neoproterozoic Allaqi Suture in southern Eastern Desert of Egypt. Further studies conducted by Amer, Kusky et al. (2010) proposed that such band color combinations are not suited to identify the contact between serpentinite and ophiolitic metagabbro and metabasalts, nor can they be used to differentiate grey granite from pink granite.
However for our case in NorthEast Greenland the band ratio combination image using 4/7, 4/1, 2/3 x 4/3 (Figure 26) shows good results for lithologic discrimination. This map highlights lithological units in Shannon Ø, which are not presented in current geological maps, and helps to better define lithological boundaries specifically in Wollaston Forland and Clavering Ø.

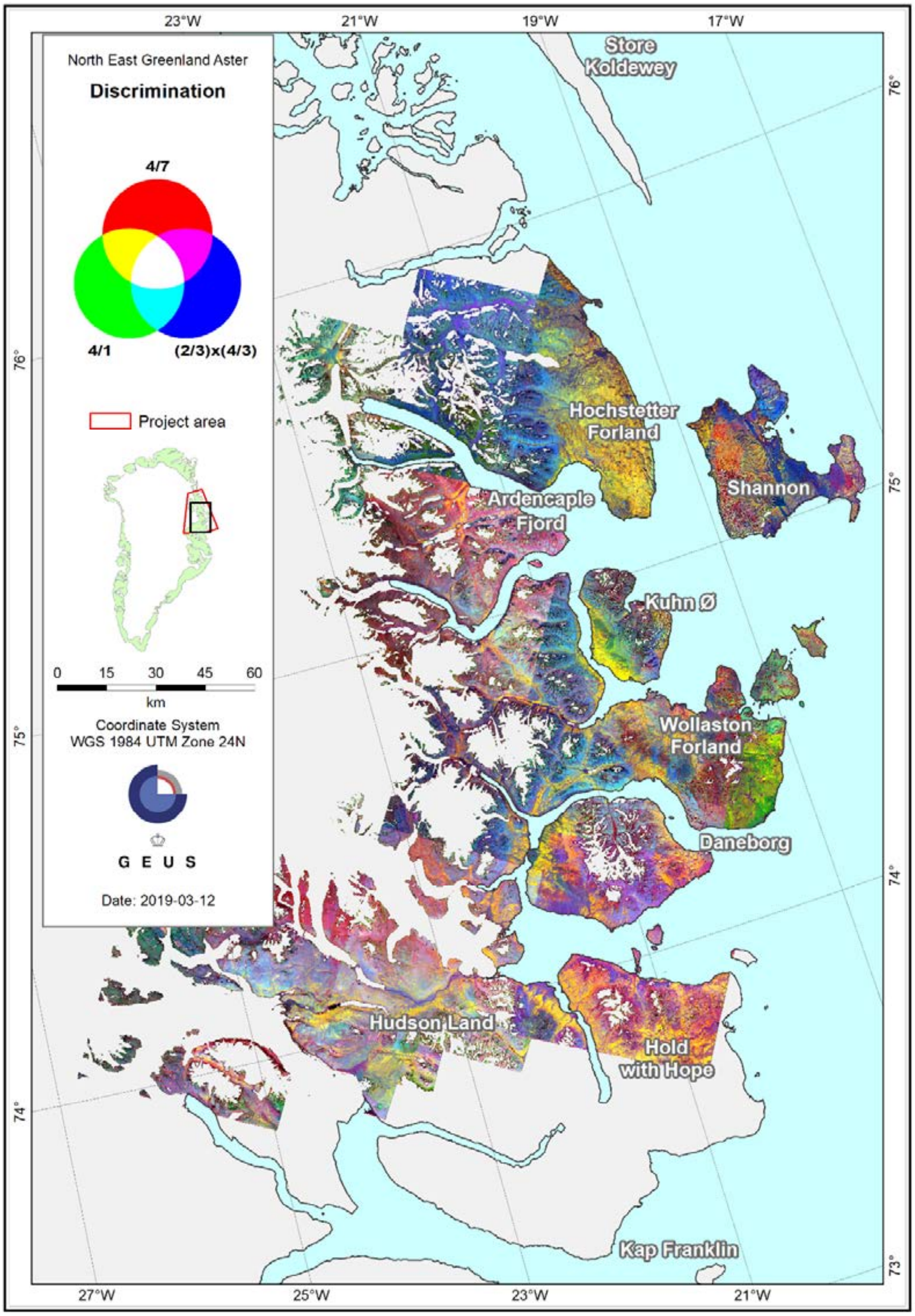

Figure 26. RGB false color composite image of ASTER band ratios, highlighting different lithological units. Red: B4/B7, Green: B4/B1, Blue: B2/B3 x B4/B3

4.4.5 Enhanced structural features

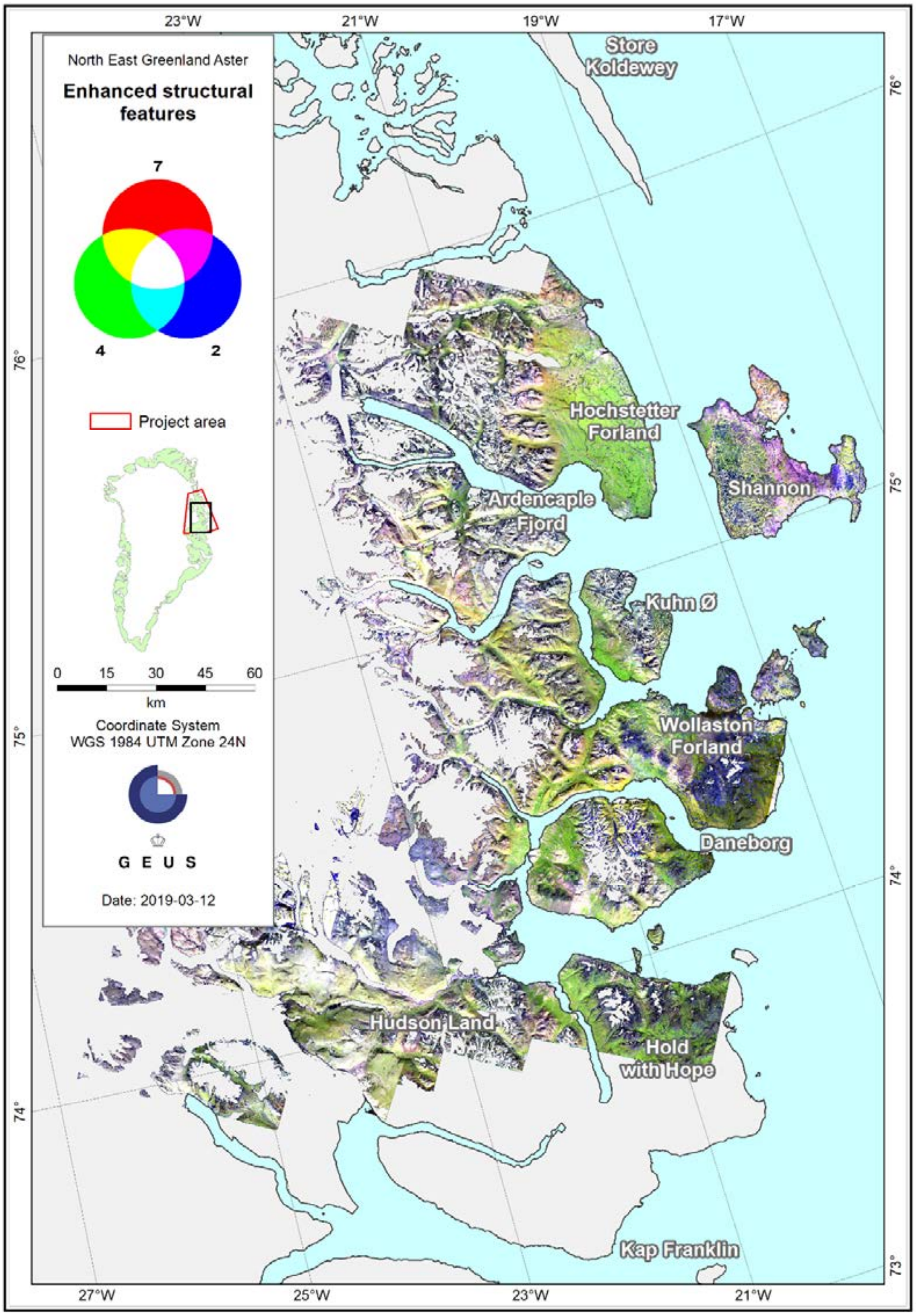

Figure 27. RGB false color composite image enhancing mineral groups and other surface features. Red: B7, Green: B4, Blue: B2

The purpose of this false color composite image (Red: Band 7, Green: Band 4, Blue: Band 2) is to enable the visual discrimination of mineral groups and other surface features.

Green pixels indicate stronger absorption in the ASTER bands 2 and 7 relative to band 4. This can be related to minerals with Al(Fe)-OH or bounded water SWIR absorptions (clays and white micas). Green color mainly corresponds to quaternary rocks in the geological map. Carbonate minerals more likely have a light purple color, but chlorite, epidote and (or) amphiboles with ferric/ferrous iron absorptions more likely have yellowish colors. White pixels are related to high-albedo surfaces, which may contain clays and (or) micas. Basalts (The Lower Plateau Lava Series, mostly aphyric quartz tholeiites) and orthogneiss rocks in the geological map correlate with dark purple and pink colors, respectively.

5. Geodatabase and Greenland Web-Portal

The band ratio and band ratio color combination results obtained from processing of ASTER data are exported from ENVI in a GeoTiff format. By using an ArcGIS Model Builder iterate setup, the raster data is imported with a batch process into an ESRI file geodatabase. All files are then projected to the same coordinate system (i.e. WGS 84 UTM Zone 24 North, EPSG 32624). In ArcGIS v. 10.6.1 each image is then displayed by using a bilinear interpolation and by blanking out the black background values. No stretch type or gamma has been applied.

The ArcGIS project is hosted as a Web Map Service on GEUS' ArcGIS Servers and deployed on the official Greenland Portal (Figure 28). For each ASTER band ratio and band color combination image on the portal, a color legend has been added describing relative abundance of associated mineral compositions (low to high) and the RGB color representation for a combined group of indices, respectively. A metadata description is added as well that provides origins of the data and contact persons.

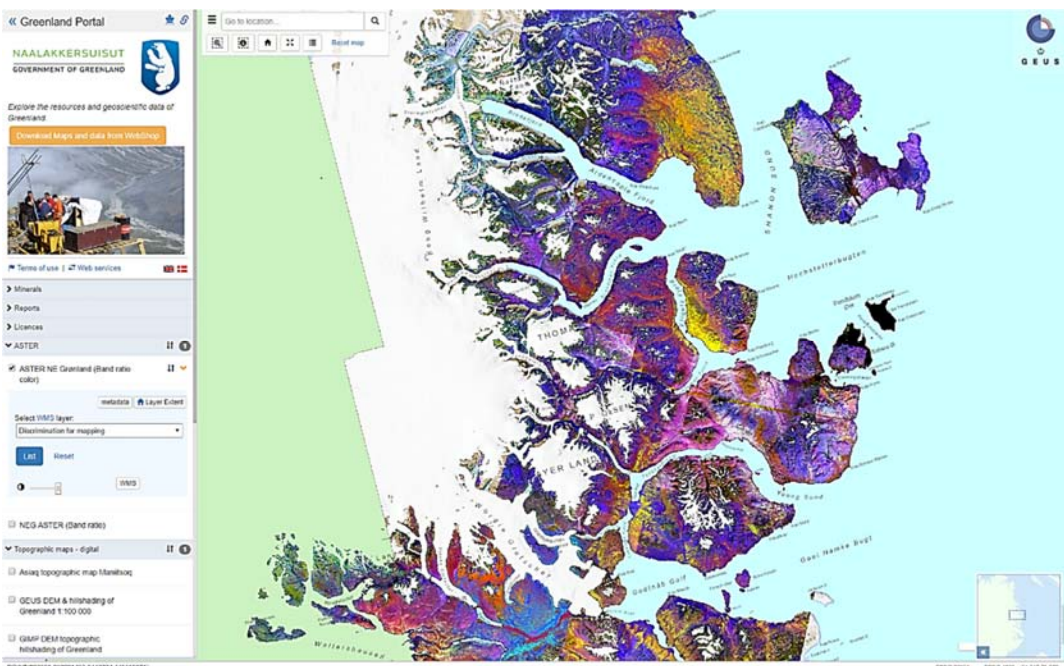

Figure 28. Data access through the Greenland Web-portal[5]

[5] http://data.geus.dk/geusmap/?mapname=greenland_portal

6. Conclusion

1. ASTER data can be used to discriminate between minerals that are spectrally similar in certain wavelengths (e.g. calcite and chlorite in the SWIR), but spectrally different in other wavelengths (e.g. calcite-bearing carbonate rocks and chlorite-bearing rocks in the TIR).
2. Mathematical operators and transformations such as band ratio color combinations, band ratios, PCA and MNF applied to the ASTER image data obtained semi-qualitative estimations of the lithological units.
3. Band ratios of ASTER reflectance data successfully generated relative abundance image products for mineral groups including AlOH, MgOH/carbonate, and those bearing ferrous iron (e.g., chlorite).
4. Due to coarse spatial resolution of ASTER data (particularly the TIR subsystem and to a lesser extent the SWIR subsystem with a 90 and 30 m spatial resolution, respectively), the mixture of signatures from various components (such as multiple lithologies or lichen and vegetation covered outcrops) within individual pixels can weaken/mask certain diagnostic mineral features and/or change their wavelength positions in the SWIR range (Salehi, Rogge et al. 2017). In other words, band ratios do not indicate the occurrence of a mineral with absolute certainty or with any idea of quantity. Therefore, it is essential to perform ground truthing and use other available data such as geological maps and geochemical and petrological datasets in conjunction with ASTER data.
5. Band ratios generated using only two (broad) bands can be strongly affected by effects of background minerals and overlapping features. Caution must be taken when interpreting the related index maps.
6. Cloud cover, vegetation and atmospheric effects can alter surface reflectance as recorded by the sensor. These features should be corrected and encountered prior to performing any mapping approach.
7. Using other spaceborne data (e.g Sentinel-2) to provide large-scale reconnaissance mapping of geologic materials is recommended for future investigations over vast arctic regions where field access is limited. The results presented in (Salehi, Mielke et al. 2019) can be used as a starting point for such initiatives.

7. References

Abdeen, M. M., et al. (2001). Application of ASTER band-ratio images for geological mapping in arid regions: the neoproterozoic Allaqi Suture, Egypt. Proceedings of GSA 2001 Annual Meeting. Boston.

Abdelsalam, M. and R. Stern (1999). "Mineral exploration with satellite remote sensing imagery: Examples from the Neoproterozoic Arabian-Nubian Shield." Journal of African Earth Sciences **28**(4): 1.

Abdelsalam, M. G., et al. (2000). "Mapping gossans in arid regions with Landsat TM and SIR-C images: the Beddaho Alteration Zone in northern Eritrea." Journal of African Earth Sciences **30**(4): 903-916.

Amer, R., et al. (2010). "Lithological mapping in the Central Eastern Desert of Egypt using ASTER data." Journal of African Earth Sciences **56**(2-3): 75-82.

Bierwirth, P. (2002). "Evaluation of ASTER satellite data for geological applications." Consultancy Report to Geoscience Australia.

Christoffersen, M. and H. F. Jepsen (2007). Geological maps of North and North East Greenland 1:250 000. Copenhagen, Geological Survey of Denmark and Greenland.

Clark, R. N., et al. (2007). "USGS digital spectral library splib06a." US geological survey, digital data series **231**: 2007.

Di Tommaso, I. and N. Rubinstein (2007). "Hydrothermal alteration mapping using ASTER data in the Infiernillo porphyry deposit, Argentina." Ore Geology Reviews **32**(1-2): 275-290.

Duke, E. F. (1994). "Near infrared spectra of muscovite, Tschermak substitution, and metamorphic reaction progress: implications for remote sensing." Geology **22**(7): 621-624.

Escher, J. C. (2001). Geological map of Greenland, Kong Oscar Fjord 1:500 000 scale, Sheet 11. Copenhagen Geological Survey of Denmark and Greenland.

Gad, S. and T. Kusky (2006). "Lithological mapping in the Eastern Desert of Egypt, the Barramiya area, using Landsat thematic mapper (TM)." Journal of African Earth Sciences **44**(2): 196-202.

Gasmi, A., et al. (2016). "PCA and SVM as geo-computational methods for geological mapping in the southern of Tunisia, using ASTER remote sensing data set." Arabian Journal of Geosciences **9**(20): 753.

Gomez, C., et al. (2005). "Using ASTER remote sensing data set for geological mapping, in Namibia." Physics and Chemistry of the Earth, Parts A/B/C **30**(1-3): 97-108.

Green, A. A., et al. (1988). "A transformation for ordering multispectral data in terms of image quality with implications for noise removal." IEEE Transactions on geoscience and remote sensing **26**(1): 65-74.

Harpøth, O. (1986). The mineral occurrences of central East Greenland, Kommissionen for Videnskabelige Undersøgelse i Grønland.

Henriksen, N. (1997). Geological map of Greenland, Dove Bugt 1:500 000 scale, Sheet 10. Copenhagen, Geological Survey of Denmark and Greenland.

Henriksen, N. (2003). Caledonian orogen of East Greenland 70 N–82 N: Geological map at 1: 1,000,000. Copenhagen, Geological Survey of Denmark and Greenland.

Henriksen, N. (2009). Greenland from Archaean to Quaternary: Descriptive Text to the 1995 Geological Map of Greenland 1: 2 5000 000, Geological Survey of Denmark and Greenland, Ministry of Climate and Energy.

Hewson, R., et al. (2004). Assessment of ASTER imagery for geological mapping within the Broken Hill and Olary domains. Proceedings of the 12-th Australasian Remote Sensing and Pho togrammetric Conference.

Hewson, R., et al. (2005). "Seamless geological map generation using ASTER in the Broken Hill-Curnamona province of Australia." Remote Sensing of Environment **99**(1-2): 159-172.

Hewson, R., et al. (2015). "Using the Geoscience Australia-CSIRO ASTER maps and airborne geophysics to explore Australian geoscience." Journal of Spatial Science **60**(2): 207-231.

Higgins, A., et al. (2008). The Greenland Caledonides: Evolution of the northeast margin of Laurentia, Geological Society of America.

Hunt, G. R. (1977). "Spectral signatures of particulate minerals in the visible and near infrared." Geophysics **42**(3): 501-513.

Jensen, J. R. (2015). Introductory digital image processing: a remote sensing perspective, Prentice Hall Press.

Kalinowski, A. and S. Oliver (2004). "ASTER mineral index processing manual." Remote Sensing Applications, Geoscience Australia **37**: 36.

Larsen, L. M., et al. (2014). "Eocene to Miocene igneous activity in NE Greenland: northward younging of magmatism along the East Greenland margin." Journal of the Geological Society **171**(4): 539-553.

Larsen, P.-H., et al. (2008). "The Devonian basin in East Greenland—Review of basin evolution and vertebrate assemblages." The Greenland Caledonides: Evolution of the Northeast Margin of Laurentia: Geological Society of America Memoir **202**: 273-292.

Pournamdari, M., et al. (2014). "Spectral transformation of ASTER and Landsat TM bands for lithological mapping of Soghan ophiolite complex, south Iran." Advances in Space Research **54**(4): 694-709.

Rowan, L. C., et al. (2003). "Mapping hydrothermally altered rocks at Cuprite, Nevada, using the Advanced Spaceborne Thermal Emission and Reflection Radiometer (ASTER), a new satellite-imaging system." Economic Geology **98**(5): 1019-1027.

Rowan, L. C. and J. C. Mars (2003). "Lithologic mapping in the Mountain Pass, California area using advanced spaceborne thermal emission and reflection radiometer (ASTER) data." Remote Sensing of Environment **84**(3): 350-366.

Rowan, L. C., et al. (2005). "Lithologic mapping of the Mordor, NT, Australia ultramafic complex by using the Advanced Spaceborne Thermal Emission and Reflection Radiometer (ASTER)." Remote Sensing of Environment **99**(1-2): 105-126.

Salehi, S. (2018). Potentials and challenges for hyperspectral mineral mapping in the Arctic: Developing innovative strategies for data acquisition and integration department of geosciences and natural resource management. Copenhagen university, Copenhagen university. **PhD**.

Salehi, S. (2018). Potentials and challenges for hyperspectral mineral mapping in the Arctic: Developing innovative strategies for data acquisition and integration, Department of Geosciences and Natural Resource Management, Faculty of ….

Salehi, S., et al. (2018). "Integration of Vessel-Based Hyperspectral Scanning and 3D-Photogrammetry for Mobile Mapping of Steep Coastal Cliffs in the Arctic." Remote Sensing **10**(2): 175.

Salehi, S., et al. (2019). "Comparison of ASTER and Sentinel-2 datasets for geological mapping: A case study from North-East Greenland." Geological Survey of Denmark and Greenland Bulletin: In press.

Salehi, S., et al. (2017). "Modeling and assessment of wavelength displacements of characteristic absorption features of common rock forming minerals encrusted by lichens." Remote Sensing of Environment **199**: 78-92.

Salehi, S. and S. M. Thaarup (2018). "Mineral mapping by hyperspectral remote sensing in West Greenland using airborne, ship-based and terrestrial platforms." Geological Survey of Denmark and Greenland Bulletin **41**: 47-50.

Sønderholm, M. and H. Tirsgaard (1993). Lithostratigraphic framework of the Upper Proterozoic Eleonore Bay Supergroup of East and North-East Greenland, Grønlands geologiske undersøgelse.

Testa, F., et al. (2018). "Lithological and hydrothermal alteration mapping of epithermal, porphyry and tourmaline breccia districts in the Argentine Andes using ASTER imagery." Remote Sensing **10**(2): 203.

Thorning, L., et al. (2019). Remote Sensing in Greenland, Overview of selected mineral resources remote sensing activities 1979 – 2017. Geological Survey of denmark and Greenland. **in prep**.

Tirsgaard, H. and M. Sønderholm (1997). Lithostratigraphy, sedimentary evolution, and sequence stratigraphy of the Upper Proterozoic Lyell Land Group (Eleonore Bay Supergroup) of east and north-east Greenland, Geological Survey of Denmark.

Upton, B. and C. Emeleus (1977). "The Tertiary geology of Hold With Hope, northern East Greenland." Rapport Grønlands Geologiske Undersøgelse **85**: 115-121.

Volesky, J. C., et al. (2003). "Geological control of massive sulfide mineralization in the Neoproterozoic Wadi Bidah shear zone, southwestern Saudi Arabia, inferences from orbital remote sensing and field studies." Precambrian Research **123**(2-4): 235-247.

Wahi, M., et al. (2013). "ASTER VNIR & SWIR band enhancement for lithological mapping-a case study of the Azegour Area (Western High Atlas, Morocco)." ASTER **3**(12).

Watt, W. S. (1994). "Stratigraphy and correlation of the Tertiary plateau basalts in North-East Greenland." Grønlands Geologiske Undersøgelse, Rapport **162**: 185-194.

Appendix 1 Standard ASTER band ratios after Kalinowski and Oliver (2004)

Feature	Band or Ratio	Comments	Reference
Iron			
Ferric iron, Fe3+	2/1		Rowan
Ferrous iron, Fe2+	5/3 + 1/2		Rowan
Laterite	4/5		Bierwith
Gossan	4/2		Volesky
Ferrous silicates (biot, chl, amph)	5/4	Fe oxide Cu-Au alteration	CSIRO
Ferric oxides	4/3	Can be ambiguous [3]	CSIRO
Carbonates/mafic minerals			
Carbonate / chlorite /epi-dote	(7+9)/8		Rowan
Epidote / chlorite / amphibole	(6+9)/(7+8)	Endoskarn	CSIRO
Amphibole / MgOH	(6+9)/8	Can be either MgOH or carbonate [6]	Hewson
Dolomite	(6+8)/7		Rowan, USGS
Carbonate	13/14	Exoskarn (cal/dolom)	Bierwith, Nimoyima, CSIRO
Silicates			
Sericite / muscovite /illite / smectite	(5+7)/6	Phyllic alteration	Rowan (USGS) Hewson (CSIRO)
Alunite / kaolinite / pyrophyllite	(4+6)/5		Rowan (USGS)
Phengitic	5/6		Hewson
Muscovite	7/6		Hewson
Kaolinite	7/5	Approximate only [3]	Hewson
Clay	$(5x7)/6^2$		Bierwith
Alteration	4/5		Volesky
Host rock	5/6		Volesky
Silica			
Quartz rich rocks	14/12		Rowan
Basic degree index (gnt, cpx, epi, chl)	12/13	Exoskarn (gnt, px)	Bierwith, CSIRO
SiO2	13/12	Same as 14/12	Palomera
Siliceous rocks	(11x11)/(10x12)		Nimoyima
Silica	11/10		CSIRO
Silica	11/12		CSIRO
Silica	13/10		CSIRO
Other			
NDVI	(3-2)/(3+2)	Normalised difference vegetation index	

[6] Comments from Hewson, R., et al. (2004). Assessment of ASTER imagery for geological mapping within the Broken Hill and Olary domains. Proceedings of the 12-th Australasian Remote Sensing and Pho togrammetric Conference.

Appendix 2 Common band ratio color combination

Features	Red	Green	Blue	Reference
Vegetation and visible bands	3, 3/2, or NDVI	2	1	
AlOH minerals/advanced argillic alteration[7]	5/6 (phen)	7/6 (musc)	7/5 (kaol)	Hewson (CSIRO)
Clay, amphibole, laterite	$(5x7)/6^2$ (clay)	6/8 (amph)	4/5 (lat)	Bierwith
Gossan, alteration, host rock	4/2 (goss)	4/5 (alt)	5/6 (host)	Volesky
Gossan, alteration, host rock	6 (goss)	2 (alt)	1 (host)	
Decorellation (envi)	13	12	10	Bierwith
Silica, carbonate, basic degree index	(11x11)/10/12 (silica)	13/14 (carb)	12/13 (basic)	Bierwith
Silica	11/10	11/12	13/10	CSIRO
Discrimination for mapping	4/1	3/1	12/14	Abdelsalam
Discrimination	4/7	4/1	(2/3)x(4/3)	Sultan
Discrimination	4/7	4/3	2/1	Abrams (USGS)
Silica, Fe2+	14/12	(1/2) + (5/3)	MNF Band 1	Rowan (USGS)
Enhanced structural features	7	4	2	Rowan (USGS)

[7] Alunite/Pyrophyllite, Mica, Kaolinite/Dickite

Appendix 3 Downloaded ASTER scenes covering the initial project area[8]

No.	File name	Sub-Area name
1	**AST_L1T_00307092004141407_20150505041445_24950.hdf**	**Hudson Land**
2	**AST_L1T_00307112004140203_20150505045325_64899.hdf**	**Hudson Land**
3	**AST_L1T_00307112004140212_20150505045334_42792.hdf**	**Hudson Land**
4	**AST_L1T_00307242006140757_20150515105343_60807.hdf**	**Hudson Land**
5	**AST_L1T_00307242006140806_20150515105340_83495.hdf**	**Hudson Land**
6	**AST_L1T_00308012003140745_20150430083214_32277.hdf**	**Hudson Land**
7	**AST_L1T_00308072003133033_20150430101321_105114.hdf**	**Hudson Land**
8	**AST_L1T_00308072003133042_20150430101321_105109.hdf**	**Hudson Land**
9	**AST_L1T_00308072003133050_20150430101329_112684.hdf**	**Hudson Land**
10	**AST_L1T_00308102000141036_20150410225811_29774.hdf**	**Hudson Land**
11	**AST_L1T_00308102000141045_20150410225815_82201.hdf**	**Hudson Land**
12	**AST_L1T_00308102000141053_20150410225813_37460.hdf**	**Hudson Land**
13	**AST_L1T_00308102000141102_20150410225821_29887.hdf**	**Hudson Land**
14	**AST_L1T_00308132006134322_20150515173024_69838.hdf**	**Hudson Land**
15	**AST_L1T_00308132006134340_20150515173024_69842.hdf**	**Hudson Land**
16	**AST_L1T_00308132006134349_20150515173016_39300.hdf**	**Hudson Land**
17	**AST_L1T_00308252002135148_20150424145009_69100.hdf**	**Hudson Land**
18	**AST_L1T_00308302004134909_20150505205603_105794.hdf**	**Hudson Land**
19	**AST_L1T_00308302004134918_20150505205603_105791.hdf**	**Hudson Land**
20	**AST_L1T_00308302004134926_20150505205604_112849.hdf**	**Hudson Land**
21	**AST_L1T_00307112004140146_20150505045324_42338.hdf**	**Hudson Land**
22	**AST_L1T_00307112004140155_20150505045317_41977.hdf**	**Hudson Land**
23	AST_L1T_00307302005220845_20150510132612_81382.hdf	Hudson Land
24	AST_L1T_00307042006223932_20150515034738_115025.hdf	Hudson Land
25	AST_L1T_00307052004143859_20150505025313_86060.hdf	Hudson Land
26	AST_L1T_00307052004143908_20150505025258_85367.hdf	Hudson Land
27	AST_L1T_00307052004143917_20150505025258_85364.hdf	Hudson Land
28	AST_L1T_00307052007144544_20150520041155_56147.hdf	Hudson Land
29	AST_L1T_00307052007144553_20150520041155_56159.hdf	Hudson Land
30	AST_L1T_00307062002140427_20150423044048_101271.hdf	Hudson Land
31	AST_L1T_00307092004141416_20150505041445_24948.hdf	Hudson Land
32	AST_L1T_00307112004140221_20150505045334_42788.hdf	Hudson Land
33	AST_L1T_00307132006223332_20150515070736_116395.hdf	Hudson Land
34	AST_L1T_00307192005222701_20150510094818_62891.hdf	Hudson Land
35	AST_L1T_00307192005222710_20150510094818_62889.hdf	Hudson Land
36	AST_L1T_00307192005222719_20150510094823_63034.hdf	Hudson Land
37	AST_L1T_00307272000135900_20150410155541_106841.hdf	Hudson Land
38	AST_L1T_00307282001140435_20150501104623_51013.hdf	Hudson Land

[8] ASTER scenes highlighted in bold indicate the final dataset selected for processing

No.	File name	Sub-Area name
39	AST_L1T_00307302005220854_20150510132612_81387.hdf	Hudson Land
40	AST_L1T_00308012003140754_20150430083214_32288.hdf	Hudson Land
41	AST_L1T_00308082002225339_20150424034330_49567.hdf	Hudson Land
42	AST_L1T_00308082002225348_20150424034333_118026.hdf	Hudson Land
43	AST_L1T_00308102000141111_20150410225818_21354.hdf	Hudson Land
44	AST_L1T_00308112000145403_20150410232602_98998.hdf	Hudson Land
45	AST_L1T_00308112000145412_20150410232601_98965.hdf	Hudson Land
46	AST_L1T_00308112000145421_20150410232602_99000.hdf	Hudson Land
47	AST_L1T_00308132006134358_20150515173016_39308.hdf	Hudson Land
48	AST_L1T_00308132006134406_20150515173016_39310.hdf	Hudson Land
49	AST_L1T_00308142007135653_20150520233447_89250.hdf	Hudson Land
50	AST_L1T_00308142007135701_20150520233457_89843.hdf	Hudson Land
51	AST_L1T_00308192000140509_20150411041658_64081.hdf	Hudson Land
52	AST_L1T_00308192000140518_20150411041658_64087.hdf	Hudson Land
53	AST_L1T_00308252002135206_20150424145016_106984.hdf	Hudson Land
54	AST_L1T_00308302004134953_20150505205600_112542.hdf	Hudson Land
55	AST_L1T_00306122003142014_20150429125756_97337.hdf	Dove Bugt
56	AST_L1T_00306122003142022_20150429125802_31610.hdf	Dove Bugt
57	AST_L1T_00306172004145014_20150504211952_30580.hdf	Dove Bugt
58	AST_L1T_00306272001211633_20150418015117_51315.hdf	Dove Bugt
59	AST_L1T_00306282004143145_20150505004308_19263.hdf	Dove Bugt
60	AST_L1T_00306282004143153_20150505004309_87174.hdf	Dove Bugt
61	AST_L1T_00306282004143202_20150505004313_87346.hdf	Dove Bugt
62	AST_L1T_00307012002215255_20150423025101_14327.hdf	Dove Bugt
63	AST_L1T_00307012005210146_20150510033811_63449.hdf	Dove Bugt
64	AST_L1T_00307012005210154_20150510033816_105599.hdf	Dove Bugt
65	AST_L1T_00307022001150446_20150418050747_43387.hdf	Dove Bugt
66	AST_L1T_00307022004140747_20150505015211_15830.hdf	Dove Bugt
67	AST_L1T_00307022004140755_20150505015211_15828.hdf	Dove Bugt
68	AST_L1T_00307022004140804_20150505015211_15824.hdf	Dove Bugt
69	AST_L1T_00307032001221733_20150418061046_121917.hdf	Dove Bugt
70	AST_L1T_00307052004143806_20150505025302_57348.hdf	Dove Bugt
71	AST_L1T_00307052004143815_20150505025313_86048.hdf	Dove Bugt
72	AST_L1T_00307052004143823_20150505025313_86058.hdf	Dove Bugt
73	AST_L1T_00307052004143832_20150505025313_86054.hdf	Dove Bugt
74	AST_L1T_00307092004141358_20150505041503_21434.hdf	Dove Bugt
75	AST_L1T_00307092004141407_20150505041445_24950.hdf	Dove Bugt
76	AST_L1T_00307112001145840_20150418092530_60834.hdf	Dove Bugt
77	AST_L1T_00307112004140146_20150505045324_42338.hdf	Dove Bugt
78	AST_L1T_00307112004140155_20150505045317_41977.hdf	Dove Bugt
79	AST_L1T_00307112005213809_20150510070433_52260.hdf	Dove Bugt
80	AST_L1T_00307112005213818_20150510070433_52265.hdf	Dove Bugt
81	AST_L1T_00307112005213827_20150510070433_52267.hdf	Dove Bugt
82	AST_L1T_00307122001140320_20150418101240_37562.hdf	Dove Bugt

No.	File name	Sub-Area name
83	AST_L1T_00307122001140329_20150418101243_16578.hdf	Dove Bugt
84	AST_L1T_00307122001140338_20150418101242_37574.hdf	Dove Bugt
85	AST_L1T_00307122001140347_20150418101246_68516.hdf	Dove Bugt
86	AST_L1T_00307122001140356_20150418101259_18188.hdf	Dove Bugt
87	AST_L1T_00307122001140405_20150418101253_16789.hdf	Dove Bugt
88	AST_L1T_00307142000142936_20150410091353_24587.hdf	Dove Bugt
89	AST_L1T_00307202003215008_20150430051001_71729.hdf	Dove Bugt
90	AST_L1T_00307202003215017_20150430051008_30434.hdf	Dove Bugt
91	AST_L1T_00307202003215026_20150430051011_72404.hdf	Dove Bugt
92	AST_L1T_00307242006140757_20150515105343_60807.hdf	Dove Bugt
93	AST_L1T_00307272000135816_20150410155521_55436.hdf	Dove Bugt
94	AST_L1T_00307272000135825_20150410155520_55426.hdf	Dove Bugt
95	AST_L1T_00307282001140400_20150501104602_45190.hdf	Dove Bugt
96	AST_L1T_00307302001215906_20150501132527_87140.hdf	Dove Bugt
97	AST_L1T_00308012003140710_20150430083148_33868.hdf	Dove Bugt
98	AST_L1T_00308072003133033_20150430101321_105114.hdf	Dove Bugt
99	AST_L1T_00308102000141000_20150410225813_37474.hdf	Dove Bugt
100	AST_L1T_00308102000141009_20150410225811_29765.hdf	Dove Bugt
101	AST_L1T_00308102000141036_20150410225811_29774.hdf	Dove Bugt
102	AST_L1T_00308102000141045_20150410225815_82201.hdf	Dove Bugt
103	AST_L1T_00308112000145319_20150410232556_9159.hdf	Dove Bugt
104	AST_L1T_00308132006134322_20150515173024_69838.hdf	Dove Bugt
105	AST_L1T_00308252002135121_20150424145009_69079.hdf	Dove Bugt
106	AST_L1T_00308252002135130_20150424145009_69096.hdf	Dove Bugt
107	AST_L1T_00308302004134842_20150505205554_112440.hdf	Dove Bugt
108	AST_L1T_00308302004134851_20150505205554_112438.hdf	Dove Bugt
109	AST_L1T_00308302004134900_20150505205603_105796.hdf	Dove Bugt
110	AST_L1T_00308302004134909_20150505205603_105794.hdf	Dove Bugt
111	AST_L1T_00308302004134918_20150505205603_105791.hdf	Dove Bugt
112	AST_L1T_00307012002215304_20150423025101_14329.hdf	Dronning Louise Land
113	AST_L1T_00307012002215313_20150423025056_107672.hdf	Dronning Louise Land
114	AST_L1T_00307012002215321_20150423025131_109393.hdf	Dronning Louise Land
115	AST_L1T_00307022002142757_20150423030913_114463.hdf	Dronning Louise Land
116	AST_L1T_00307022002142806_20150423030913_114464.hdf	Dronning Louise Land
117	AST_L1T_00307022002142815_20150423030923_115941.hdf	Dronning Louise Land
118	AST_L1T_00307032001221751_20150418061058_31517.hdf	Dronning Louise Land
119	AST_L1T_00307102003211430_20150430020404_18298.hdf	Dronning Louise Land
120	AST_L1T_00307112005213836_20150510070443_52690.hdf	Dronning Louise Land
121	AST_L1T_00307202003215035_20150430051012_65010.hdf	Dronning Louise Land
122	AST_L1T_00307202003215044_20150430051011_64947.hdf	Dronning Louise Land
123	AST_L1T_00307202003215053_20150430051021_74123.hdf	Dronning Louise Land
124	AST_L1T_00307262005142533_20150510120702_50973.hdf	Dronning Louise Land